deg/min, typical half-height peak width = 0.14° ω, 3 standards collected 41 times, 3% fluctuation, 1% variation in azimuth scan, no absorption correction, 398 duplicates, 2.0% R-merge, 5930 unique reflections with $I \geq 3.0\sigma(I)$). The structure was solved by automated Patterson analysis (PHASE). The asymmetric unit consists of half a tetracation lying on an inversion center together with two triflate anions. The structure was refined by full-matrix least squares on F using scattering factors from the International Tables for X-ray Crystallography, Vol. IV,[34] including anomalous terms for Ru and S, and weights $\propto [\sigma^2(I) + 0.0009I^2]^{-1/2}$. With use of 451 parameters, C, Ru, S, F, and O were refined anisotropically; all hydrogen atoms were fixed. The final R was 0.035 (R_w = 0.038) with the error of fit being 1.40 and maximum Δ/σ = 0.13. The largest residual density was 1.52 e/Å^3 near Ru1.

Acknowledgment. We thank Ronald J. Davis and William Marshall for capable technical assistance.

Registry No. 1, 113860-02-9; **2**, 113860-07-4; **3a**, 99617-73-9; **3b**, 118397-71-0; **3c**, 118397-72-1; **3d**, 118397-73-2; **3e**, 118397-75-4; **3f**, 118397-77-6; *syn*-**4**, 118397-89-0; *anti*-**4**, 118456-61-4; **5** $(C)^{4+}(OTf^-)_4$, 118397-93-6; **5** $(Si)^{4+}(OTf^-)_4$, 118397-95-8; **5** $(Ge)^{4+}(OTf^-)_4$, 118417-84-8; **5** $(Sn)^{4+}(OTf^-)_4$, 118417-86-0; **5** $(Pb)^{4+}(OTf^-)_4$, 118417-88-2; Cp^*RuCl_2, 92390-47-1; AgO_3SCF_3, 2923-28-6; $[(Cp^*Ru)_2(\eta^6,\eta^6\text{-}[2_2]\text{-}1,4\text{-cyclophane})]^{2+}(OTf^-)_2$, 118397-79-8; $[(Cp^*Co)(\eta^6\text{-}[2_2]\text{-}1,4\text{-cyclophane})]^{2+}(OTf^-)_2$, 118397-80-1; Cp^*CoCl_2, 118397-98-1; $[(Cp^*Ru)(\eta^6,\eta^6\text{-}[2_2]\text{-}1,4\text{-cyclophane})CoCp^*]^{3+}(OTf^-)_3$, 118397-82-3; $[(\eta^6\text{-}[2_2]\text{-}1,4\text{-cyclophane})_2Ru]^{2+}(OTf^-)_2$, 118397-83-4; $\{[Cp^*Ru(\eta^6,\eta^6\text{-}[2_2]\text{-}1,4\text{-cyclophane})]_2Ru\}^{4+}(OTf^-)_4$, 118397-85-6; $[Cp^*Ru(\eta^6\text{-triptycene})]^+OTf^-$, 118397-87-8; $[(Cp^*Ru)_3(\eta^6,\eta^6,\eta^6\text{-triptycene})]^{3+}(OTf^-)_3$, 118397-91-4; $\{[Cp^*Ru(\eta\text{-}C_6H_5)]_3(C_6H_5)Sb\}^{4+}(OTf^-)_4$, 118417-92-8; $\{[Cp^*Ru(\eta\text{-}C_6H_5)]_4B\}^{3+}(OTf^-)_3$, 118397-97-0; $\{[Cp^*Ru(p\text{-}CH_3O\text{-}\eta\text{-}C_6H_4\text{-}O)]_6C_6\}^{6+}(OTf^-)_6$, 118681-49-5; $[(Cp^*Ru)_4(\eta^6,\eta^6,\eta^6,\eta^6\text{-}p\text{-quaterphenyl})]^{4+}(OTf^-)_4$, 118417-90-6; $[(Cp^*Ru)_6(\eta^6,\eta^6,\eta^6,\eta^6,\eta^6,\eta^6\text{-}p\text{-sexiphenyl})]^{6+}(OTf^-)_6$, 118681-50-8; $(\eta^4\text{-}1,3\text{-cyclohexadiene})Ru(\eta^6\text{-}[2_2]\text{-}1,4\text{-cyclophane})$, 90590-75-3; trifluoromethanesulfonic acid, 1493-13-6; tetraphenylantimonium bromide, 21450-52-2; tetraphenylantimonium trifluoromethanesulfonate, 104316-49-6; sodium tetraphenylborate, 143-66-8.

Supplementary Material Available: X-ray data (tables of atomic positional parameters, thermal parameters, H atom fixed fractional coordinates, intra- and intermolecular non-bonding distances, bond distances and bond angles involving H atoms, bond distances and bond angles for the O_3SCF_3 anions and CH_3NO_2 solvates) (19 pages); observed and calculated structure factors for the complexes $\{[Cp^*Ru(\eta\text{-}C_6H_5)]_4Ge\}^{4+}(OTf^-)_4$, $\{[Cp^*Ru(p\text{-}CH_3O\text{-}\eta\text{-}C_6H_4\text{-}O)]_6C_6\}(OTf)_6\cdot 6CH_3NO_2$, and $[(Cp^*Ru)_4(\eta^6,\eta^6,\eta^6,\eta^6\text{-}p\text{-quaterphenyl})]^{4+}(OTf^-)_4$ (37 pages). Ordering information is given on any current masthead page.

Electrostatic Structural Enforcement in Low-Dimensional Solids: Synthesis, Structure, and Electronic Properties of Polycationic Ruthenium Complexes with Polycyanoanions

Michael D. Ward,* Paul J. Fagan,* Joseph C. Calabrese, and David C. Johnson†

Contribution No. 4748 from the Central Research and Development Department, Experimental Station 328, E. I. du Pont de Nemours & Co., Wilmington, Delaware 19880-0328.
Received May 24, 1988

Abstract: New low-dimensional solids prepared from polycyanoanions and $Cp^*Ru(\eta\text{-}C_6Me_6)^+$ (D^+: $Cp^* = C_5Me_5$), $(Cp^*Ru)_2(\eta^6,\eta^6\text{-}[2_2](1,4)\text{cyclophane})^{2+}$ ($D^+\text{-}D^+$), and $[Cp^*Ru(\eta\text{-}C_6H_5)]_4E^{4+}$ ($(D^+)_4E$: E = C, Si) demonstrate that the polycations structurally enforce the solid-state structure, with anions adopting stacking motifs that reflect the spatial distribution of charge in the polycations. The mononuclear D^+ cation forms dimorphs with $TCNQ^-$ (TCNQ = tetracyanoquinodimethane) with the empirical formula $[D^+][TCNQ^-]$. One of these (**1**) crystallizes with 1-D mixed stacks of cations and $TCNQ^-$ anions, whereas the other phase (**2**) possesses discrete $D^+A^-A^-D^+$ units with a $(TCNQ)_2^{2-}$ π-dimer situated between two cations. Segregated stacking motifs that are rather common for the $TCNQ^-$ anion are not observed. However, structural enforcement provided by the ruthenium centers in the rod-shaped $D^+\text{-}D^+$ dication affords different structural motifs in $[D^+\text{-}D^+][(TCNQ)_x^{2-}]$ (**3**, x = 2; **4**, x = 4). Nonconducting **3**, prepared by electrochemical reduction of TCNQ in the presence of the dication at −0.1 V (vs. Ag/AgCl), possesses mixed stack linear chains with alternating cations and $(TCNQ)_2^{2-}$ π-dimers, i.e., a ...$D^+\text{-}D^+A^-A^-D^+\text{-}D^+A^-A^-$... motif. In contrast, **4** crystallizes as conductive black parallelepipeds by slow electrochemical reduction of TCNQ in the presence of the dication at potentials more positive than $E^\circ_{(TCNQ/TCNQ^-)}$ and possesses two crystallographically unique TCNQ stacks parallel to the long axes of the cations. The distance between cationic Ru sites in $D^+\text{-}D^+$ accommodates four TCNQ molecules with an overall (2−) charge; the resultant mixed valent ρ = 0.5 stacks afford a room temperature conductivity of 0.2 Ω^{-1} cm^{-1}. The solid-state structures of the nonconducting charge-transfer salts $[D^+\text{-}D^+]\{C_3[C(CN)_2]_3^-\}_2$ (**5**) and $[(D^+)_4E]\{C_3[C(CN)_2]_3^-\}_4\cdot x MeNO_2$ (**6**, E = C, x = 6; **7**, E = Si, x = 4) exhibit linear chains of $C_3[C(CN)_2]_3^-$ anions. For **5**, the anion stacking axis is parallel to the dications, whereas **6** and **7** possess mutually orthogonal anion stacks that are aligned parallel to the orthogonal axes defined by two pairs of cationic centers in the tetracations. Magnetic susceptibility and EPR data for **4** indicate the presence of an energetically accessible triplet state 0.08 eV above the singlet ground state with zero field splitting constants $|D|$ = 66 G and $|E|$ = 11 G. The EPR spectra of **5**–**7** also indicate the presence of energetically accessible triplet species. However, magnetic susceptibility measurements indicate strong antiferromagnetic coupling of the anion spins, suggesting that these triplet species are due to impurities or crystalline defects.

The design and synthesis of low-dimensional molecular solids[1] with desirable electronic properties requires understanding of the factors that affect the formation of different structural phases, coupled with elucidation of the structure–function relationships in these materials. Whereas numerous organic charge transfer solids have been reported,[2] we have been investigating new materials derived from organometallic reagents with emphasis on

* Author to whom correspondence should be addressed.
† Present Address: Department of Chemistry, University of Oregon, Eugene, OR 97403.

(1) *Extended Linear Chain Compounds*; Miller, J. S., Ed.; Plenum Press: New York, 1981–83; Vol. 1–3.
(2) Herbstein, F. H. *Perspectives in Structural Chemistry*; Dunitz, J. D., Ibers, J. A., Eds.; John Wiley and Sons: New York, 1971; Vol. IV, p 166.

0002-7863/89/1511-1719$01.50/0

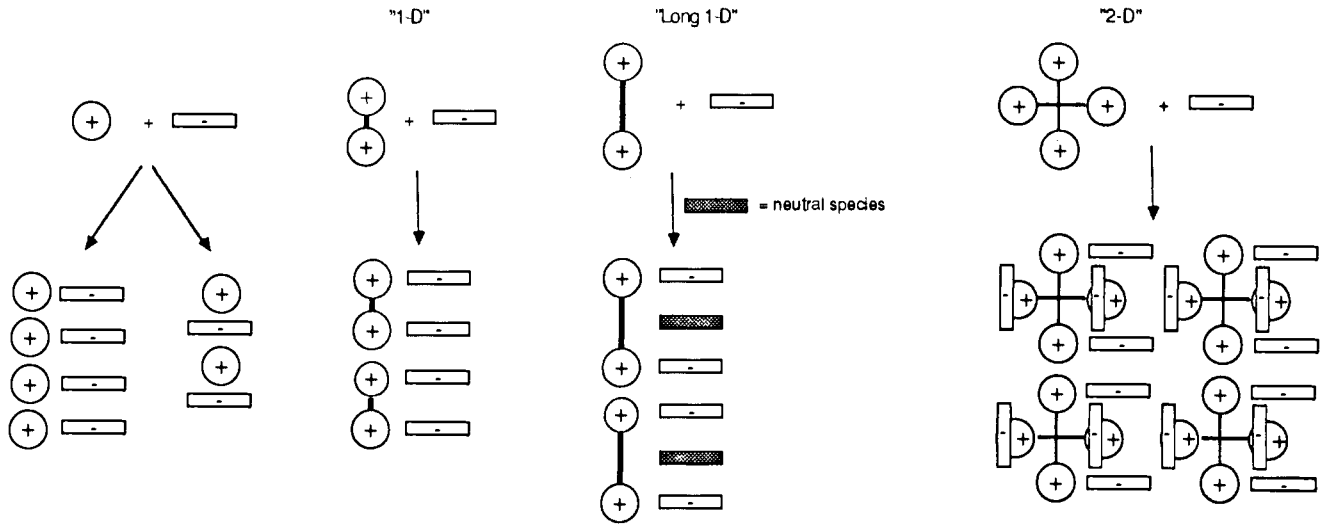

Figure 1. Schematic representation of different stacking motifs for the ruthenium polycations.

maintaining the integrity of the organometallic component. The diverse physical and chemical properties of organometallic complexes promise rational and systematic modification of the properties of charge transfer solids, such as crystal packing, donor–acceptor (DA) interactions, stoichiometry, and degree of band filling. The utility of organometallic reagents in charge transfer solids has been demonstrated in a limited way with $(Cp^*)_2Fe^+$ ($Cp^* = C_5Me_5$),[3-5] $(C_6H_5CH_3)_2Cr^+$,[6,7] $(Cp)Fe(arene)^+$ ($Cp = C_5H_5$; arene = $C_6Me_3H_3$, C_6Me_6),[8] and $(\eta\text{-arene})_2M^{2+}$ (M = Fe, Ru, arene = $C_6Me_3H_3$, C_6Me_6).[9,10]

One of the largest obstacles in the design of molecular solids is that control of the crystal packing can be elusive in the absence of an overt directing influence due to the role of poorly understood crystal packing forces and intermolecular interactions. One approach to controlling solid-state architecture has been illustrated by "structurally enforced" molecular materials, as exemplified by the covalently linked metallopthalocyanine rings in polymeric $[Si(Pc)O]_n$, which upon doping exhibits metallic conductivity due to π-overlap of the Pc rings.[11] Non-covalent intermolecular interactions such as hydrogen bonding[12] and Cl···Cl and C–H···O interactions[13] have also been exploited for the engineering of crystalline lattices possessing planar aromatic molecules. In the absence of guiding influence, other factors direct the solid-state motif of ionic molecular solids, not the least among them electrostatic interactions between oppositely charged ions. The polycationic ruthenium complexes described in the preceding paper,[14] specifically $Cp^*Ru(\eta\text{-}C_6Me_6)^+$ ($\mathbf{D^+}$), $(Cp^*Ru)_2(\eta^6,\eta^6\text{-}[2_2](1,4)cyclophane)^{2+}$ ($\mathbf{D^+\text{–}D^+}$), and $[Cp^*Ru(\eta\text{-}C_6H_5)]_4E^{4+}$ ($(\mathbf{D^+})_4\mathbf{E}$: E = C, Si), present a unique opportunity to examine whether these interactions can enforce the solid-state structure of molecular solids by inducing counterions to orient in motifs dictated by the spatial arrangement of positive charges.

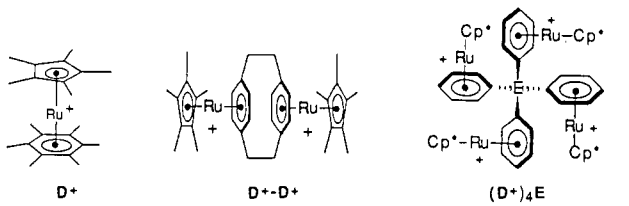

In order to pursue this strategy, we have addressed the effect of these cations on the stacking motifs of polycyanoanion acceptor molecules, which tend to align in linear chains due to their planarity and intermolecular π–π interactions. This is conceptually illustrated in Figure 1. The crystal packing of solids with the mononuclear cation $\mathbf{D^+}$ would be expected to be unpredictable and difficult to control. However, the two positive charges confined along the rodlike axis of a $\mathbf{D^+\text{–}D^+}$ dication may, by electrostatic attraction forces, induce alignment of the planar anions during crystallization into 1-D anion aggregates parallel to the molecular axis of the dication. Ordering of the anions into extended linear arrays in the bulk crystal can be realized by favorable π–π interactions between anions, culminating in a solid-state motif that reflects the initial ion pair interactions. Extension of this principle to $(\mathbf{D^+})_4\mathbf{E}$ suggests that planar anions may stack parallel to the axes defined by the pairs of dipositive charge, resulting in two mutually orthogonal 1-D chains and a "**2-D**" motif. One can also envision modification of the electronic properties by variation in the number of, and distance between, cationic centers, which would control molecular stoichiometry and interplanar spacing between anions. For example, changing the distance between charged centers in a dication can afford inclusion of "neutral" cyano acceptors, resulting in mixed valent anion stacks, as depicted for the "long 1-D" dication in Figure 1.

We report herein results from our initial investigations of the synthesis, structure, and physical characterization of charge transfer solids derived from these cations and the $TCNQ^-$ and $C_3[C(CN)_2]_3^-$ polycyanoanions. The solid-state motifs of the acceptor anion stacks and the molecular stoichiometry of the complexes are governed by the spatial orientation of charges in the polycations, which significantly affects the intermolecular interactions and electronic properties of these materials. It has also been demonstrated that the selectivity toward different materials during their electrochemical synthesis can be directed by careful control of experimental parameters during electrochemical crystal growth of these materials.

(3) (a) Reis, A. H., Jr.; Preston, L. D.; Williams, J. M.; Peterson, S. W.; Candela, G. A.; Swartzendruber, L. J.; Miller, J. S. *J. Am. Chem. Soc.* **1979**, *101*, 2756. (b) Miller, J. S.; Reis, A. H., Jr.; Candela, G. A. Quasi One-Dimensional Conductors II. *Lecture Notes in Physics*; *1978*; Springer-Verlag: New York, 1979; Vol. 96, p 313.
(4) Miller, J. S.; Reis, A. H., Jr.; Gebert, E.; Ritsko, J. J.; Salaneck, W. R.; Kovnat, L.; Cape, T. W.; Van Duyne, R. P. *J. Am. Chem. Soc.* **1979**, *101*, 711.
(5) Ritsko, J. J.; Nielsen, P.; Miller, J. S. *J. Chem. Phys.* **1977**, *67*, 687.
(6) Shibaeva, R. P.; Atovmyan, L. O.; Rozenberg, L. P. *Chem. Commun.* **1969**, 649.
(7) Shibaeva, R. P.; Atovmyan, L. O.; Orfanova, M. N. *Chem. Commun.* **1969**, 1494.
(8) Lequan, R-M.; Lequan, M.; Jaouen, G.; Ouahab, L.; Batail, P.; Padiou, J.; Sutherland, R. G. *Chem. Commun.* **1985**, 116.
(9) Ward, M. D.; Johnson, D. C. *Inorg. Chem.* **1987**, *26*, 4213.
(10) Ward, M. D. *Organometallics* **1987**, *6*, 754.
(11) (a) Schoch, K. F., Jr.; Kundalkar, B. R.; Marks, T. J. *J. Am. Chem. Soc.* **1979**, *101*, 7071. (b) Dirk, C. W.; Marks, T. J. *Inorg. Chem.* **1984**, *23*, 4325.
(12) Panunto, T. W.; Urbanczyk-Lipkowska, Z.; Johnson, R.; Etter, M. C. *J. Am. Chem. Soc.* **1987**, *109*, 7786.
(13) Sarma, J. A. R. P.; Desiraju, G. R. *Acc. Chem. Res.* **1986**, *19*, 222.
(14) Fagan, P. J.; Ward, M. D.; Calabrese, J. C. *J. Am. Chem. Soc.*, preceding paper in this issue.

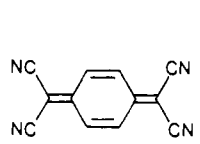

TCNQ

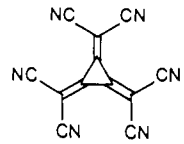

$C_3[C(CN)_2]_3$

Results

TCNQ Complexes with $Cp^*Ru(\eta\text{-}C_6Me_6)^+$ (D^+). Synthesis. Charge transfer complexes are commonly prepared by in situ electron transfer between donor and acceptors. However, cyclic voltammetry in acetonitrile indicated that the 18-e⁻ D^+ cation was reduced only beyond the solvent limit ($E < -2.5$ V vs Ag/AgCl) and isolation of the neutral 19-e⁻ complex was not possible. The very negative potential required for reduction of D^+ ensures that the monocation will be stable in the presence of most organic acceptor anions, including $TCNQ^-$, and accordingly, metathesis routes were employed for the synthesis of CT complexes.

When $(n\text{-}Bu_4N^+)(TCNQ^-)$ was added to solutions of D^+ a slightly soluble emerald green precipitate $[D^+][TCNQ^-]$ (**1**) formed immediately. Crystal growth by slow diffusive mixing of these components gave **1** as a fibrous polycrystalline solid accompanied by very small amounts (<5%) of a purple crystalline solid **2** with the same empirical formula. The colors of **1** and **2** were reminiscent of those observed for the $[Cp^*_2Fe^+][TCNQ^-]$ "1-D" phase and the $[Cp^*_2Fe^+]_2[TCNQ^-]_2$ "dimer" phase,[3,4] respectively, in which the different colors are attributed to the presence of the isolated $TCNQ^-$ anion and a $(TCNQ)_2^{2-}$ dimer. The infrared spectra of **1** revealed ν_{CN} absorptions at 2151 and 2176 cm^{-1}, similar to ν_{CN} observed for the $[Cp^*_2Fe^+][TCNQ^-]$ "1-D" phase. For **2**, ν_{CN} = 2151, 2182 cm^{-1}, consistent with the presence of the $(TCNQ)_2^{2-}$ dimer.

Since it was not possible to prepare crystals of **1** suitable for X-ray structural analysis by conventional methods, an alternative approach was used. We have recently reported that electrocrystallization is an attractive method for the synthesis of high-quality crystals of poorly conducting as well as conducting materials.[9,15] Reduction of TCNQ ($E^\circ_{(TCNQ/TCNQ^-)}$ = +0.22 V vs Ag/AgCl) at platinum electrodes at +0.3 V in acetonitrile in the presence of D^+ afforded crystals of **1** at the electrode surface suitable for X-ray analysis, with no evidence of **2** (eq 2). It is interesting to note that although the conducting $\rho = 0.5$ complex $[(C_5H_5)Fe(\eta\text{-}C_6Me_6)^+][(TCNQ)_2^-]$ (ρ = degree of charge per TCNQ molecule) has been reported,[8] attempts here to prepare the analogous $[D^+](TCNQ)_2^-]$ by either conventional or electrochemical means were not successful (vide infra).

$$TCNQ^- + D^+ \rightarrow [D^+][TCNQ^-] \quad \begin{matrix}\mathbf{1}\text{ (1-D phase) +} \\ \mathbf{2}\text{ (dimer phase)}\end{matrix} \qquad (1)$$

$$TCNQ + e^- \xrightarrow[E_{app} = +0.3\text{ V}]{D^+} [D^+][TCNQ^-] \quad \mathbf{1}\text{ (1-D phase)} \qquad (2)$$

Single-Crystal Structure of 1. The green phase **1** crystallized in the $P\bar{1}$ space group and possessed one-dimensional mixed stacks of D^+ and $TCNQ^-$ (A^-); i.e. a...$D^+A^-D^+A^-D^+A^-$... motif (Figure 2). The cations were found to be disordered, resulting in an apparent superposition of the Cp* and C_6Me_6 rings. The bond lengths and angles for the isolated $TCNQ^-$ anion of **1** are similar to those reported for the singly reduced anions in the $[Cp^*_2Fe^+][TCNQ^-]$ "1-D" phase[4] and RbTCNQ[16] and are readily distinguished from the bond lengths in TCNQ (Table I).[17] The planes of the $TCNQ^-$ anions and either the Cp* or C_6Me_6 ligands are essentially parallel with only a small dihedral angle of 3.00 ± 1.43°. The distance between these planes is 3.55 Å, suggesting only weak van der Waals interactions.[18] If the extended stacks are viewed perpendicular to the chain axis with translation along the *a* axis, alternating sheets of cations and anions are observed. Conversely, translation along the other two axes results in a solid-state packing arrangement wherein the anions are flanked by the organometallic cations, suggesting favorable electrostatic interactions.

Single-Crystal Structure of 2. The purple dimer phase **2** crystallized in the $P2_1/c$ space group and possessed discrete one-dimensional $D^+A^-A^-D^+$ fragments arranged in a herringbone motif (Figure 2). The Cp* ring was found to contain a 2-fold rotational disorder, similar to $[Cp^*_2Fe^+]_2[TCNQ^-]_2$.[3] The structure of the cation, determined from this complex, has been discussed in detail in the preceding paper.[14]

The average bond distances for the $TCNQ^-$ anions in **2** (Table I) are consistent with values reported for other singly reduced anions. The anions exist as a $(TCNQ)_2^{2-}$ dimer symmetrically located between two cations. The intradimer separation between $TCNQ^-$ planes is 3.13 Å, which is substantially less than the 3.5–3.6 Å van der Waals separation.[19–21] The ring planes are essentially parallel with only a small dihedral angle of 0.24°, and the anions are slightly boat shaped due to bending of the $C(CN)_2$ planes away from the dimer (the $C(CN)_2$ planes form angles of 8.97° and 9.78 with the quinoid ring plane). The dimer exhibits ring–ring overlap with one of the rings slipped approximately 1.02 Å along the short axis of the $TCNQ^-$ anion. The interplanar separation and the extent of slippage is similar to that observed for the discrete dimers present in other TCNQ complexes, e.g., $[(\eta\text{-}C_6Me_6)_2Fe][TCNQ]_2$,[10] $[Cp^*Fe]_2[TCNQ]_2$[3], $Nb_3Cl_6(C_6Me_6)_3(TCNQ)_2$,[22] and $[Pt(NH_3)_4][TCNQ]_2$.[23]

The solid-state structure shows that in each dimeric unit the two C_6Me_6 rings of the D^+ cations are parallel to and stacked face-to-face about the $(TCNQ)_2^{2-}$ dimer so that one of the methylidene carbon atoms of the TCNQ anion lies nearly in the center of the C_6 ring. The interplanar separation between the hexamethylbenzene ligand and the $TCNQ^-$ anion is 3.57 Å. It is interesting to note that only the C_6Me_6 ring faces the $(TCNQ)_2^{2-}$ dimer. This may be due to lesser repulsion forces incurred when $(TCNQ)_2^{2-}$ faces the formally neutral C_6Me_6 rather than the more anionic Cp* ring, or the more favorable electrostatic attraction between the $(TCNQ)_2^{2-}$ dimer and Ru^+ resulting from the smaller Ru–C_6Me_6 distance compared to the Cp*–Ru distance.

TCNQ Complexes with $(Cp^*Ru)_2(\eta^6,\eta^6\text{-}[2_2](1,4)\text{cyclophane})^{2+}$ (D^+–D^+). Synthesis. Cyclic voltammetry of D^+–D^+ in acetonitrile showed only an irreversible reduction at −2.18 V. Reduction of TCNQ at −0.1 V in acetonitrile in the presence of D^+–D^+ afforded purple crystals of $[D^+\text{–}D^+][TCNQ^-]_2$ (**3**) at the electrode surface suitable for X-ray analysis (eq 3). The highly crystalline nature and morphological habit of these compounds allowed crystal growth without passivation of the working electrode. The infrared spectrum of **3** revealed ν_{CN} absorptions at 2154 and 2179 cm^{-1}, indicating the presence of a fully reduced $TCNQ^-$ anion.

In contrast, when TCNQ was reduced in the presence of the dication at $E_{app} \geq E^\circ_{(TCNQ/TCNQ^-)}$, black parallelepiped crystals of $[D^+\text{–}D^+][(TCNQ)_4^{2-}]$ (**4**) grew slowly at the electrode over periods of several days to weeks. The infrared spectrum of **4** exhibited weak ν_{CN} absorptions at 2200 cm^{-1} superimposed on significant free carrier absorption above 1800 cm^{-1}. Assuming a linear relationship between the degree of TCNQ reduction and vibrational frequencies,[24,25] this indicated the presence of partially reduced $TCNQ^{0.5-}$ species.

(15) Ward, M. D. *Inorg. Chem.* **1986**, *25*, 4444.
(16) Hoekstra, A.; Spoelder, T.; Vos, A. *Acta Crystallogr., Sect. B* **1972**, *28*, 14.
(17) Long, R. E.; Sparks, R. A.; Trueblood, K. N. *Acta Crystallogr.* **1965**, *18*, 932.
(18) Bondi, A. *J. Phys. Chem.* **1964**, *68*, 441.
(19) Soos, Z. G. *Annu. Rev. Phys. Chem.* **1974**, *25*, 121.
(20) Offen, H. W. *J. Chem. Phys.* **1965**, *42*, 430.
(21) Mayerle, J. J.; Torrance, J. B.; Crowley, J. I. *Acta Crystallogr.* **1979**, *B35*, 2988.
(22) Goldberg, S. Z.; Spivack, B.; Stanley, G.; Eisenberg, R.; Braitsch, D. M.; Miller, J. S.; Abkowitz, M. *J. Am. Chem. Soc.* **1977**, *99*, 110.
(23) Endres, H.; Keller, H. J.; Moroni, W.; Nothe, D.; Dong, V. *Acta Crystallogr.* **1978**, *B34*, 1703.
(24) Van Duyne, R. P.; Cape, T. W.; Suchanski, M. R.; Siedle, A. R. *J. Phys. Chem.* **1986**, *90*, 739.
(25) Friedrich, H. B.; Person, W. B. *J. Chem. Phys.* **1966**, *44*, 2161. Jurgensen, C. W.; Peanasky, M. J.; Drickamer, H. G. *J. Chem. Phys.* **1985**, *83*, 6108.

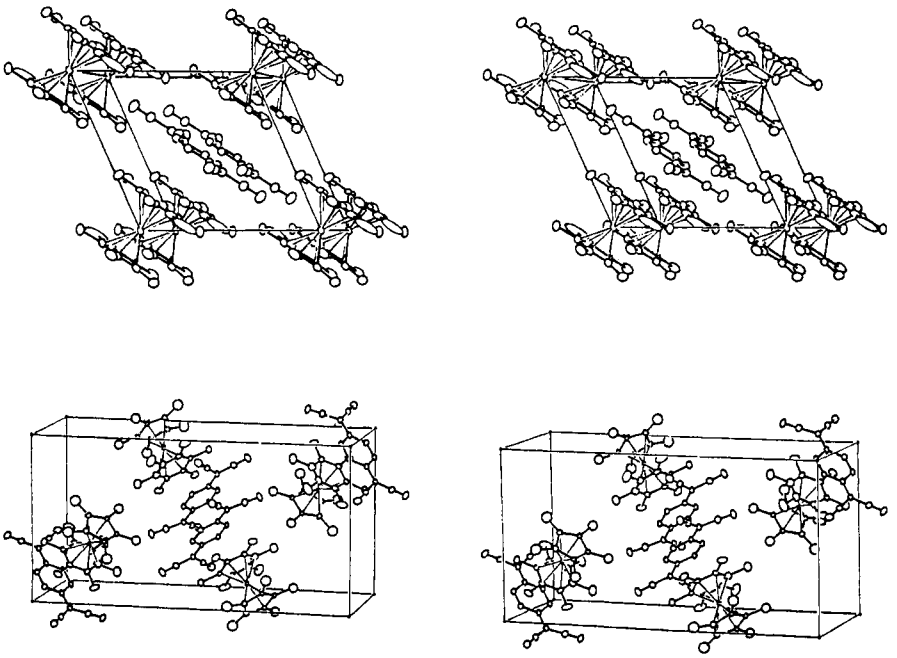

Figure 2. (Top) Stereoview of the 1-D phase **1** drawn with 20% probability ellipsoids. (Bottom) Stereoview of the dimer phase **2** drawn with 20% probability ellipsoids.

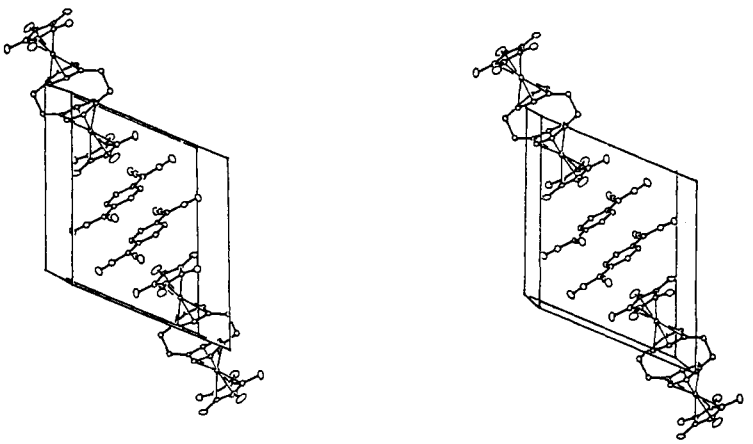

Figure 3. Stereoview of the unit cell of **3** drawn with 20% probability ellipsoids.

Table I. Average Bond Lengths for TCNQ Molecules (Å)[a]

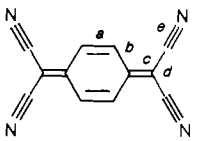

compd	*a*	*b*	*c*	*d*	*e*
1	1.369 (4)	1.414 (7)	1.424 (4)	1.418 (7)	1.143 (7)
2	1.367 (8)	1.416 (6)	1.415 (7)	1.425 (8)	1.143 (8)
3	1.377 (6)	1.408 (7)	1.423 (6)	1.425 (8)	1.126 (8)
4	1.350 (7)	1.433 (7)	1.394 (7)	1.431 (8)	1.144 (7)
	1.354 (7)	1.434 (7)	1.395 (7)	1.432 (8)	1.145 (7)
	1.341 (7)	1.440 (7)	1.385 (7)	1.435 (8)	1.140 (7)
	1.361 (7)	1.422 (7)	1.404 (7)	1.430 (8)	1.143 (7)
	1.352 (7)	1.430 (7)	1.403 (7)	1.426 (8)	1.147 (7)
	1.343 (7)	1.440 (7)	1.384 (7)	1.431 (8)	1.144 (7)
$TCNQ$[17]	1.346 (3)	1.448 (4)	1.374 (3	1.441 (4)	1.140 (1)
$RbTCNQ$[16]	1.373 (1)	1.423 (3)	1.420 (1)	1.416 (8)	1.153 (7)
$[Fe(C_5Me_5)_2^+][TCNQ^-]$[4]	1.375 (9)	1.409 (9)	1.438 (9)	1.422 (10)	1.160 (8)
$[Fe(C_6Me_6)_2^{2+}][TCNQ^-]_2$[9]	1.361 (6)	1.405 (6)	1.419 (5)	1.417 (6)	1.141 (6)
$[Ru(C_6Me_6)_2^{2+}][TCNQ^-]_2$[9]	1.374 (6)	1.414 (6)	1.428 (6)	1.415 (6)	1.151 (6)
$[Pt(NH_3)_4^{2+}][(TCNQ)_2^{2-}]$[23]	1.345 (10)	1.42	1.40 (1)	1.41 (2)	1.14 (2)
$[TPP^+][(TCNQ)_2^-]$[27]	1.354 (2)	1.434 (2)	1.396 (2)	1.428 (3)	1.17 (1)

[a] Numbers in parentheses are the average estimated standard deviations in the least significant digits.

$$\text{TCNQ} + e^- \xrightarrow[E_{app} = -0.1\text{ V}]{\mathbf{D^+}\text{-}\mathbf{D^+}} \underset{\mathbf{3}}{[\mathbf{D^+}\text{-}\mathbf{D^+}][\text{TCNQ}^-]_2} \quad (3)$$

$$\text{TCNQ} + e^- \xrightarrow[E_{app} = +0.4\text{ V}]{\mathbf{D^+}\text{-}\mathbf{D^+}} \underset{\mathbf{4}}{[\mathbf{D^+}\text{-}\mathbf{D^+}][(\text{TCNQ})_4^{2-}]} \quad (4)$$

Electrocrystallizations were terminated when the number of equivalents of TCNQ consumed reached 10% of the initial concentration. Since under these conditions $[TCNQ^0] \gg [TCNQ^-]$ in solution, the observation that **3** was the final product when crystal growth was performed at −0.1 V indicates that the two complexes are not readily interconverted, and the stoichiometry of these materials does not simply reflect the concentrations of TCNQ and $TCNQ^-$ near the end of the electrolyses. In addition, the selectivity toward either **3** or **4** at different potentials is obvious from the initial moments of crystallization as there is no visible formation of both phases at the electrode at either −0.1 or +0.4 V. When electrocrystallization was performed on large platinum foils, only a small area of the electrode was covered with crystals, indicating favorable crystal growth and a relatively small number of nucleation events. Under these conditions, simultaneous formation of both phases would have been easily observed.

Single-Crystal Structure of 3. Purple phase **3** crystallizes in the $P\bar{1}$ space group and possesses 1-D mixed stacks of $\mathbf{D^+}$–$\mathbf{D^+}$ and $(TCNQ)_2^{2-}$ dimers in a ...D^+–$D^+A^-A^-D^+$–$D^+A^-A^-$... motif (Figure 3). The bond distances and angles of the dication, determined from this complex, have been discussed in the preceding paper.[14] The $(TCNQ)_2^{2-}$ dimers are centrally located between the dications with a 3.59 Å interplanar separation between the Cp* rings and the nearest $TCNQ^-$ plane. The intradimer separation between $TCNQ^-$ planes is 3.23 Å, which is slightly greater than that observed in **2**, but similar to the intradimer separation previously observed in $[(\eta\text{-}C_6Me_6)_2M^{2+}][TCNQ^-]_2$ (M = Fe, Ru).[15] The dimer exhibits ring–ring overlap with the two $C(CN)_2$ planes bent away from the dimer by 6.42 and 6.61°, similar to that observed in **2**. However, the rings are slipped only 0.46 Å along the short axis of the TCNQ anion. The axis defined by the centroids of the two TCNQ rings is nearly colinear with the Ru–Ru axis defined by the two ruthenium atoms (1.7°) closest to the $(TCNQ)_2^{2-}$ dimer. Sheets of cations and anions are observed along the *a* axis. Along the *b* and *c* axes the $(TCNQ)_2^{2-}$ dimers and the dications form an alternating network, suggesting favorable electrostatic interactions.

Single-Crystal Structure of 4. Black complex **4** crystallized in the $P\bar{1}$ space group with two cations and eight TCNQ anions per unit cell (Figure 4). There are two half-dications lying on different centers of symmetry whose structural parameters are essentially identical with those of the cation in **3**, and two half-TCNQ molecules also related by centers of symmetry with three TCNQ molecules in general positions. The solid-state structure of **4** consists of cations and anions that stack approximately along the *a* axis while forming alternating sheets along the *c* axis. The two unique cations have slightly different orientations, as the molecular axes of the cations defined by the Ru–Ru axes are canted at an angle of 19.5° with respect to each other. The structure is reminiscent of [bipyridinium^{2+}][$(TCNQ)_4^{2-}$],[26] in which the long molecular axis of the cation is approximately parallel to the TCNQ stacking axes.

Two unique TCNQ acceptor stacks are present in **4**, both exhibiting a "zigzag" motif. However, the two stacks exhibit different overlap motifs, periodicity of interplanar spacing and canting angle of the TCNQ planes with respect to the stacking axis (Figure 5). Both stacks can be described as possessing tetrameric units of TCNQ molecules. In stack A there is an average displacement of 0.90 Å from the *a* axis for four TCNQ molecules followed by a displacement in the opposite direction to repeat the pattern. The other stack (B) exhibits an average displacement of 0.73 Å for four TCNQ molecules followed by an equal displacement in the opposite direction. In stack A the interplanar spacing between tetramers is more significant, as stack B possesses more uniform spacing.

The average bond lengths of the TCNQ molecules are midway between those reported for TCNQ and fully reduced $TCNQ^-$ anion (Table I), consistent with the nonintegral oxidation state ($\rho = 0.5$) indicated by infrared spectroscopy. The length of the exocyclic C=C bond, which is generally most indicative of the extent of reduction of TCNQ, is 1.394 (7) Å, compared to 1.374 (3) and 1.420 (1) Å for TCNQ[22] and RbTCNQ,[21] respectively. Indeed, all the bond lengths were very similar to those reported for [TPP][$TCNQ]_2$ (TPP = tetraphenylphosphonium),[27] which formally possesses $TCNQ^{0.5-}$ anions. Although the TCNQ acceptors are crystallographically inequivalent, the structural and infrared data do not indicate charge localization in terms of discrete $TCNQ^0$ and $TCNQ^-$ species.

Complexes of Polycations with $C_3[C(CN)_2]_3^-$. Synthesis. When acetonitrile solutions of $[\mathbf{D^+}\text{-}\mathbf{D^+}]$ and $[n\text{-}Bu_4N^+]\{C_3[C(CN)_2]_3^-\}$ were slowly cooled, long purple needles of $[\mathbf{D^+}\text{-}\mathbf{D^+}]\{C_3[C(CN)_2]_3^-\}_2$ (**5**) formed (eq 5). Infrared spectroscopy was consistent with the presence of the $C_3[C(CN)_2]_3^-$ monoanion (ν_{CN} = 2192, 2208 cm^{-1}).

$$\mathbf{D^+}\text{-}\mathbf{D^+} + 2C_3[C(CN)_2]_3^- \rightarrow \underset{\mathbf{5}}{[\mathbf{D^+}\text{-}\mathbf{D^+}]\{C_3[C(CN)_2]_3^-\}^2} \quad (5)$$

Charge transfer complexes of the $C_3[C(CN)_2]_3^-$ anion with $(\mathbf{D^+})_4\mathbf{E}$ (E = C, Si, Ge) were prepared in a similar fashion, affording large block-shaped, purple crystals of $[(\mathbf{D^+})_4\mathbf{E}]\{C[C(CN)_2]_3^-\}_4 \cdot x MeNO_2$ (eq 6).

$$(\mathbf{D^+})_4\mathbf{E} + C_3[C(CN)_2]_3^- \rightarrow [(\mathbf{D^+})_4\mathbf{E}]\{C_3[C(CN)_2]_3^-\}_4 \cdot x MeNO_2 \quad (6)$$

6: E = C; $x = 6$
7: E = Si; $x = 4$

Single-Crystal Structure of 5. The charge transfer complex **5** crystallized in the monoclinic $P2_1/a$ space group and possessed 1-D segregated stacks of $\mathbf{D^+}$–$\mathbf{D^+}$ cations and $C_3[C(CN)_2]_3^-$ anions (Figure 6). The structure of the dication is identical with that described in the preceding paper.[14] The anion's structure is similar to that previously reported for its dianion,[10] as well as that found in complexes with $(\eta\text{-}C_6Me_6)_2Fe^{2+}$ and $Cp^*_2Fe^+$ (Table II).[28] The anion exhibits a planar geometry with the most notable feature being the C_{ring}–C_{ring} bond length, which is significantly shorter than that in cyclopropane.[29]

The 1-D stacks of cations are aligned parallel to the *a* axis, with a 3.76-Å spacing between Cp* rings of adjacent cations within a stack. The anions adopt a zigzag ...AA...A′A′...AA...A′A′... motif where A = $C_3[C(CN)_2]_3^-$ (Figure 7), with the stacking axis also parallel to the *a* axis. The anions are dimerized as $\{C_3[C(CN)_2]_3^-\}_2$ units, in which the anions within each dimer exhibit a mutually eclipsed conformation, while the dimers are staggered with respect to each other. The 3.28-Å *intra*dimer interplanar separation is significantly smaller than the sum of the van der Waal's radii, whereas the larger 3.58-Å *inter*dimer spacing suggests minimal interactions between dimers.

Single-Crystal Structures of 6 and 7. The solid-state motifs observed in the charge transfer complexes of $C_3[C(CN)_2]_3^-$ with $(\mathbf{D^+})_4\mathbf{E}$ differ significantly from that observed in **5**. Complex **6** crystallizes in the space group $C2/c$ and possesses mutually orthogonal $C_3[C(CN)_2]_3^-$ anion stacks. The anion stacking axes are aligned parallel to axes defined by the pairs of Ru^+ centers, Ru1–Ru2 and Ru1a–Ru2a (see atom numbering in preceding paper[14]), within each of the tetracations ($d_{Ru1\text{-}Ru2}$ = 6.294 Å). This is illustrated for **6** in Figure 8, which is a slice through several unit cells as viewed nearly normal to one of the stacks. The two stacks in this compound, identical by symmetry, are canted 45° from the *b* axis. They exhibit a tetrameric motif ...ABCD... ABCD... with rather short interplanar spacings between anions within the tetramer and a large 3.63-Å separation between tetramers (Figure 7).

(26) Eley, D. D.; Ashwell, G. J.; Wallwork, S. C.; Willis, M. R.; Woodward, J. *Ann. N.Y. Acad. Sci.* **1978**, *78*, 417.

(27) Goldstein, P.; Seff, K.; Trueblood, K. N. *Acta Crystallogr., Sect. B* **1968**, *24*, 778.

(28) Ward, M. D.; Miller, J. S. To be submitted.

(29) Jones, W. R.; Stoicheff *Can. J. Phys.* **1964**, *42*, 2259.

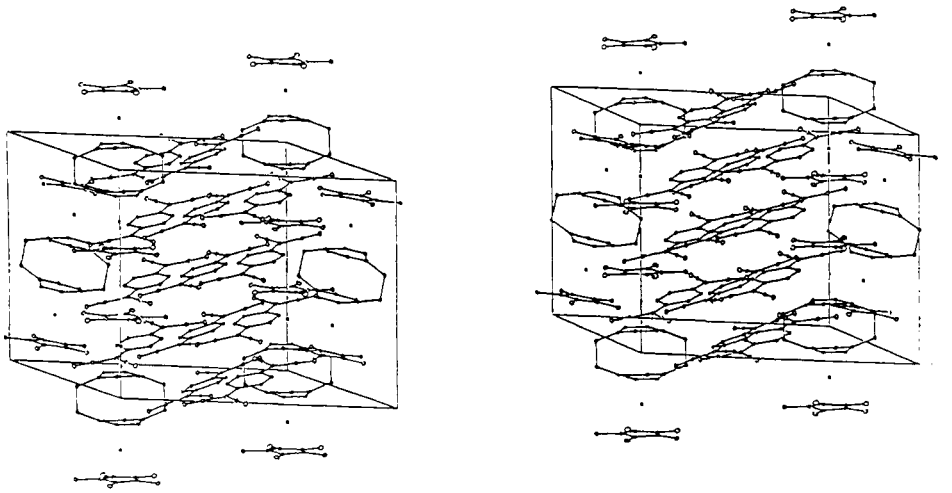

Figure 4. Stereoview of the unit cell of **4** drawn with 20% probability ellipsoids.

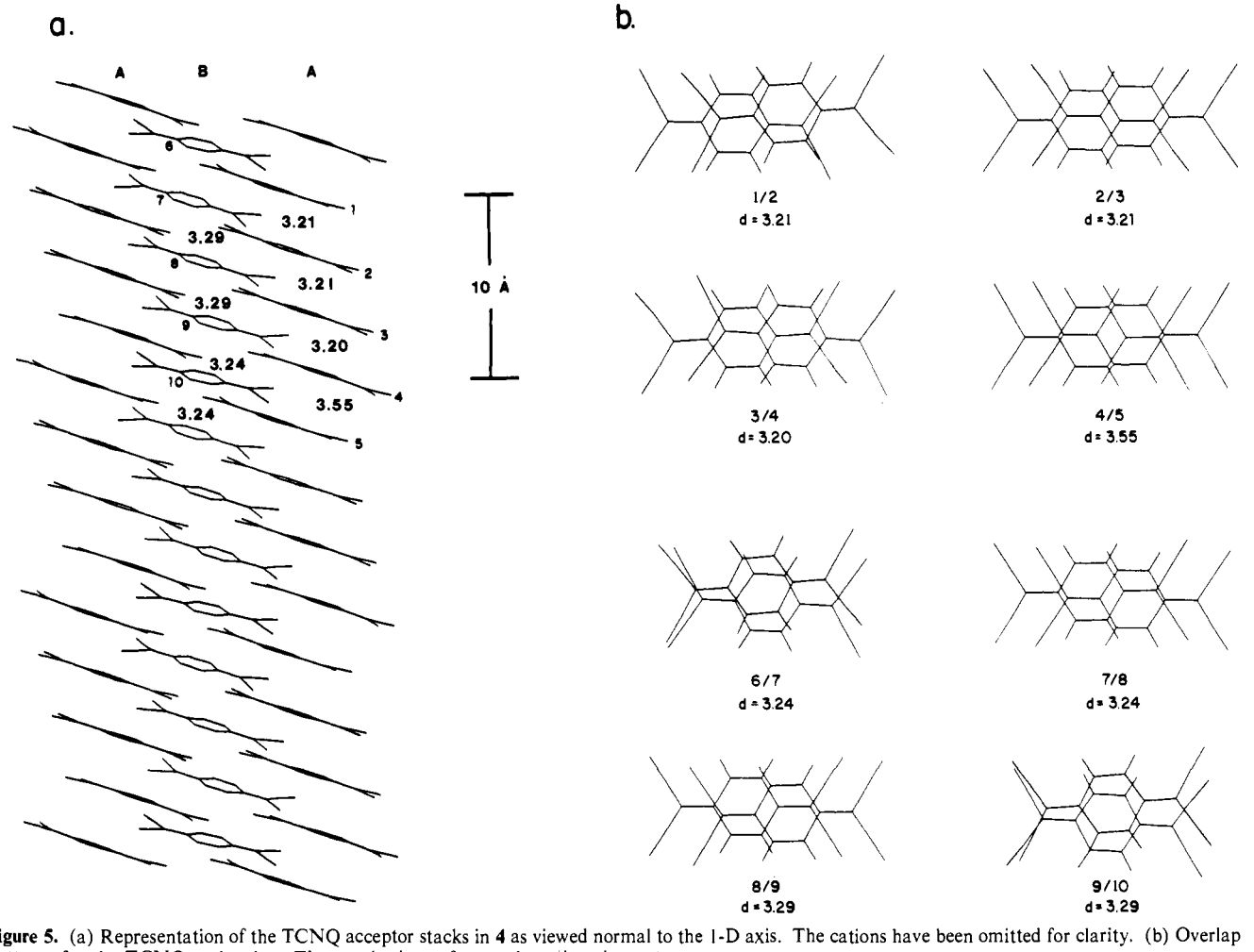

Figure 5. (a) Representation of the TCNQ acceptor stacks in **4** as viewed normal to the 1-D axis. The cations have been omitted for clarity. (b) Overlap patterns for the TCNQ molecules. The numbering refers to the anions in part a.

Similarly, **7** possesses two mutually orthogonal anion stacks with tetrameric periodicity, although it crystallizes in a lower symmetry space group, $P\bar{1}$. In this case the two stacks are unique, one aligned along the *a* axis and the other aligned in the center of the unit cell parallel to the *b* axis (Figure 9). The stack along the *a* axis is parallel to the Ru1–Ru3 axis ($d_{Ru1-Ru3}$ = 6.033 Å), whereas the stack parallel to the *b* axis is aligned along the Ru2–Ru4 axis ($d_{Ru2-Ru4}$ = 6.316 Å).

The structural features of the individual anions in **6** and **7** are not extraordinary and the bond lengths are summarized in Table II. The molecular structures of the tetracations have been discussed in the preceding paper[14] and are not discussed further here.

Electronic Properties. Conductivity. Four point probe conductivity measurements on single crystals of **1–3** and **5–7** demonstrated that these compounds were effectively insulating, with $\sigma < 10^{-6}\ \Omega^{-1}\ cm^{-1}$. However, for **4** at room temperature $\sigma = 0.2\ \Omega^{-1}\ cm^{-1}$ parallel to the stacking axis (*a* axis). The temperature dependence of conductivity for single crystals of **4** indicated activated behavior, with a broad transition centered at approximately 240 K. The activation energy for conduction was $\Delta E_a = 0.24 \pm 0.02$ eV for $T > 240$ K and $\Delta E_a = 0.38 \pm 0.03$ eV for $T < 240$ K.[30]

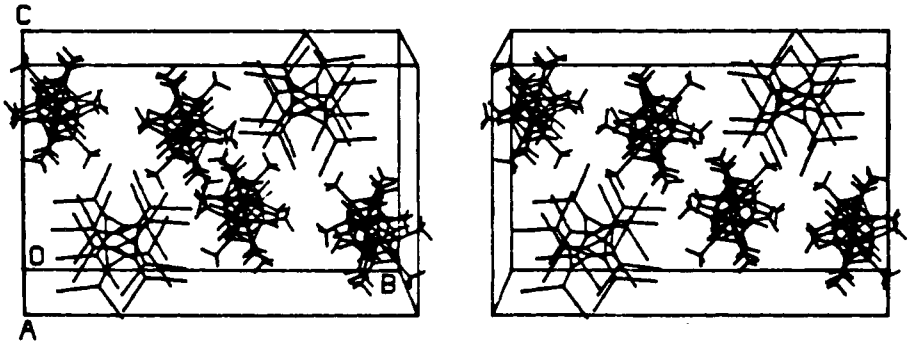

Figure 6. Stereoview of **5**.

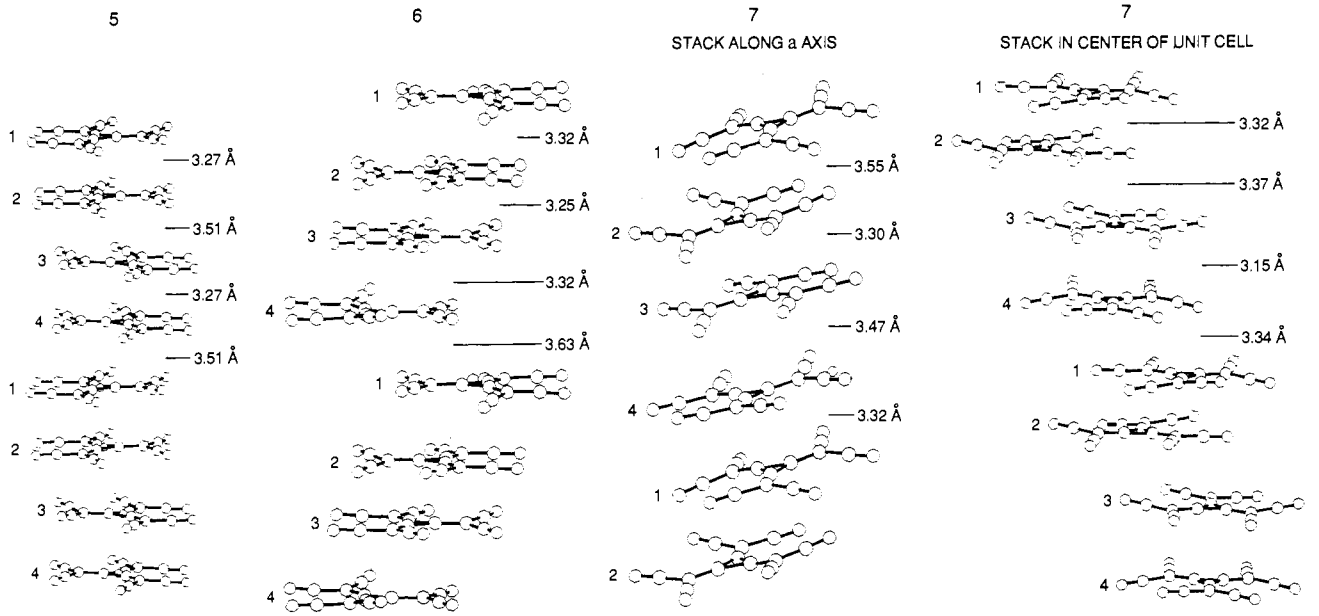

Figure 7. Stacking motifs of the $C_3[C(CN)_2]_3^-$ anions in **5**–**7**. Numbering of crystallographically identical anions in each stack and the interplanar spacings are depicted.

Table II. Average Bond Lengths in $C_3[C(CN)_2]_3^{n-}$ Anions (Å)[a]

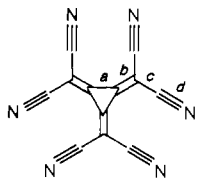

complex	*n*	*a* C_{ring}–C_{ring}	*b* C_{ring}–C_{exo}	*c* C–C	*d* C–N
5	1	1.40 (1)	1.37 (1)	1.44 (1)	1.13 (1)
6	1	1.346 (19)	1.401 (19)	1.454 (20)	1.108 (16)
7	1	1.396 (12)	1.371 (13)	1.428 (12)	1.138 (12)
$[(C_6H_3Me_3)_2Fe]\{C_3[C(CN)_2]_3\}_2$[28]	1	1.40 (1)	1.37 (1)	1.42 (1)	1.146 (9)
$[(C_5Me_5)_2Fe]\{C_3[C(CN)_2]_3\}$[28]	1	1.385 (12)	1.383 (12)	1.437 (10)	1.126 (8)
$[n\text{-}Bu_4N]_2\{C_3[C(CN)_2]_3\}$[10,28]	2	1.385 (15)	1.394 (15)	1.418 (15)	1.16 (3)
$[(C_6H_3Me_3)_2Fe]\{C_3[C(CN)_2]_3\}$[10]	2	1.38 (1)	1.39 (1)	1.42 (1)	1.10 (1)
cyclopropane[b]		1.514 (2)			

[a] Numbers in parentheses are the average estimated standard deviations in the least significant digits. [b] Jones, W. R.; Stoicheff, B. P. *Can. J. Phys.* **1964**, *42*, 2259.

Magnetic Properties. Magnetic susceptibility measurements found that **1** and **3** were diamagnetic, consistent with strong antiferromagnetic spin exchange between anions in the $(TCNQ)_2^{2-}$ dimers. However, **2**, which possesses isolated $TCNQ^-$ anions, exhibited behavior consistent with one unpaired spin of the isolated $TCNQ^-$ anion (μ_{eff} = 1.73 BM). Magnetic susceptibility measurements of **5**–**7**, which contained the $S = {}^1/_2$ $C_3[C(CN)_2]_3^-$ anion, indicated diamagnetic behavior. This strong antiferromagnetic coupling of the $C_3[C(CN)_2]_3^-$ anions is consistent with previous reports for other salts containing this anion[31] and is attributed here to the dimerization (and tetramerization) of the

(30) The activation energy was determined from data in the two temperature regimes using $\sigma = \sigma_0 \exp(-\Delta E_a/kT)$.

(31) (a) Abrahams, S. C.; Bair, H. E.; DiSalvo, F. J.; Marsh, P.; Deuring, L. A. *Phys. Rev. B* **1984**, *29*, 1258. (b) LePage, T. J.; Breslow, R. *J. Am. Chem. Soc.* **1987**, *109*, 6412.

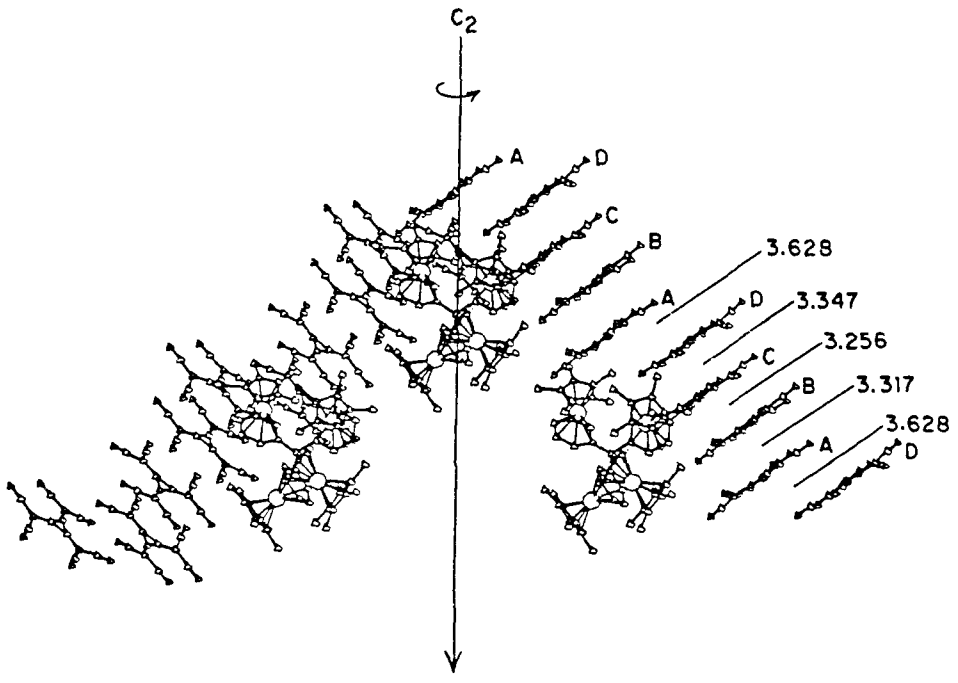

Figure 8. Representation of two orthogonal $C_3[C(CN)_2]_3^-$ anion stacks with their nearest $(D^+)_4E$ tetracation in **6** as viewed nearly normal to the *ab* plane.

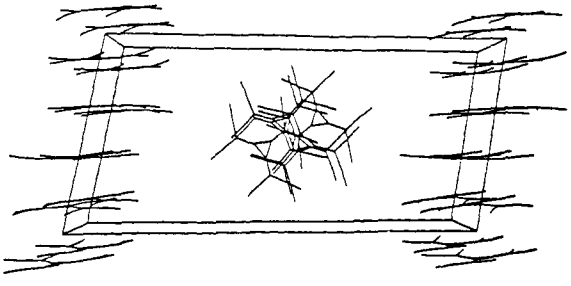

Figure 9. Unit cell of **7** illustrating the two unique $C_3[C(CN)_2]_3^-$ stacks. Note that the stacking axes are mutually perpendicular with one stack coinciding with the *a* axis and the other aligned parallel to the *b* axis in the center of the unit cell.

anions as seen from the X-ray structures.

The molar susceptibility, χ, of **4** increased with increasing temperature (Figure 10), with zero susceptibility near 100 K. This behavior is consistent with the presence of a singlet ground state and low-lying triplet excited state. For a singlet–triplet system, χ behaves according to the Bleaney–Bowers equation[32] (eq 7), where N is Avagadro's number, $\mathbf{g}$ is the isotropic g factor, μ_B is the Bohr Magneton, and ΔE_{S-T} is the singlet–triplet energy gap.

$$\chi = (N\mathbf{g}^2\mu_B^2/kT)[3 + \exp(\Delta E_{S-T}/kT)]^{-1} \qquad (7)$$

For sufficiently large values of $\Delta E_{S-T}/kT$, $\chi \propto [\exp(-\Delta E_{S-T}/kT)]/T$. Accordingly, a plot of ln χ T vs T^{-1} yields a straight line with a slope equivalent to $\Delta E_{S-T} = 0.080 \pm 0.005$ eV. This activation energy predicts approximately 5% population of the triplet state at room temperature, in accord with the observed susceptibility for **4** at this temperature.

The EPR spectrum of **4** at room temperature exhibited a single sharp $\Delta m = \pm 1$ line at 2.007410 (peak width at half-height = 1 G). Upon cooling, this signal broadened until at 175 K triplet fine structure was observed (Figure 11). The $\Delta m = \pm 1$ triplet fine structure at low temperature is attributed to the presence of randomly oriented triplets,[33] which are observable only at low T where the triplet population is small enough so that exchange

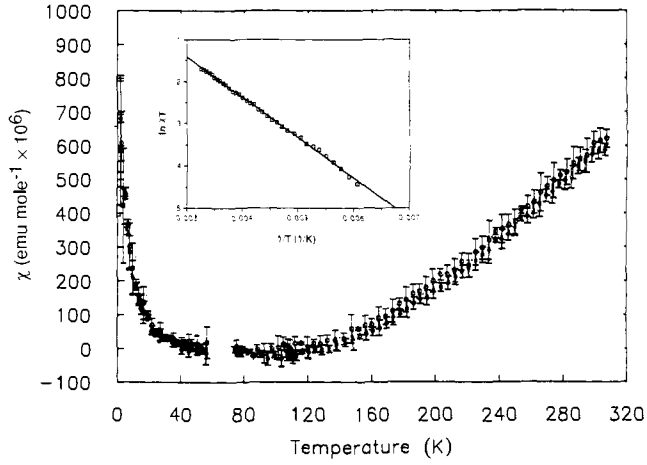

Figure 10. Magnetic susceptibility data for **4**. Inset: plot of ln χT vs $1/T$ used to determine the singlet–triplet separation.

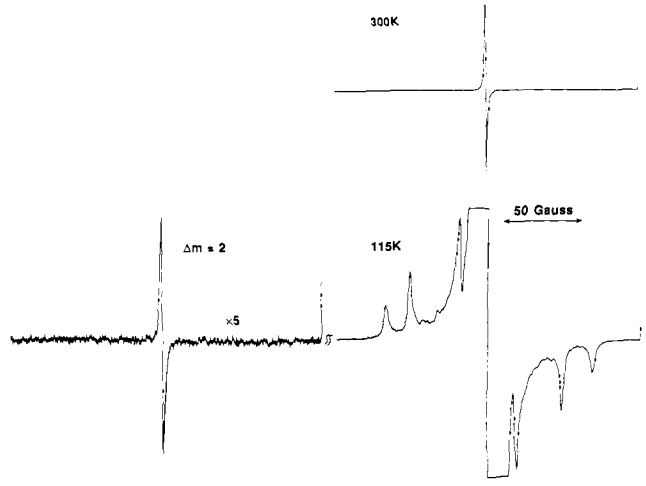

Figure 11. EPR spectra of finely divided powder of **4** at 300 and 120 K. The center line g value is 2.007410.

broadening due to triplet exciton collisions is minimized. The half-field $\Delta m = \pm 2$ resonance at 1675 G was also observed at

(32) Carlin, R. L. *Magnetochemistry*; Springer-Verlag: New York, 1986; p 75.

(33) Wasserman, E.; Snyder, L. C.; Yager, W. A. *J. Chem. Phys.* **1964**, *41*, 1763.

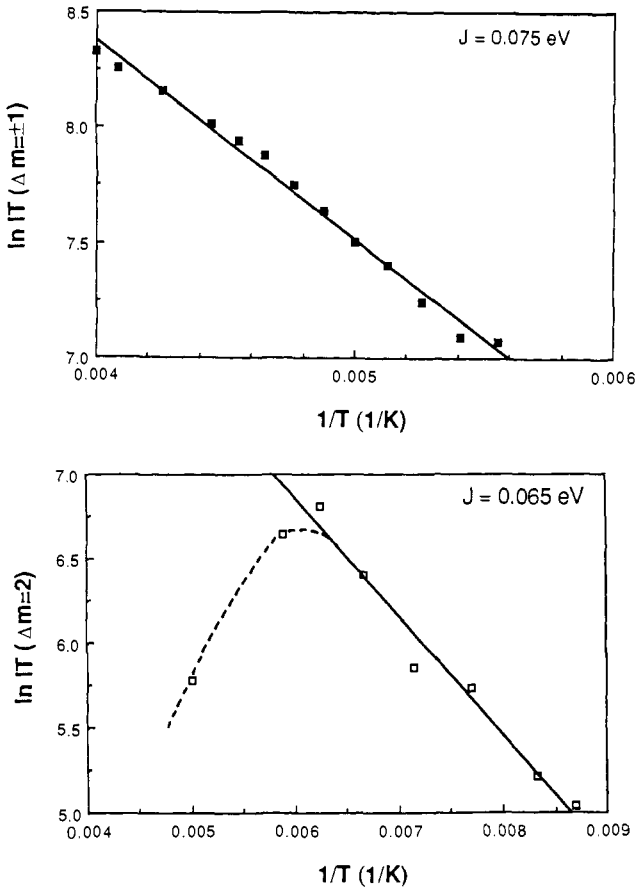

Figure 12. Intensity dependences on temperature of the $\Delta m = \pm 1$ and ± 2 transitions. EPR data between 170 and 250 K ($\Delta m = \pm 1$) were used to determine the singlet–triplet separation energy in order to obviate errors due to doublet impurities (<0.5% from Figure 10) that would contribute significantly at lower temperatures. At higher temperatures the $\Delta m = \pm 2$ transition decreases due to exciton collisions.

low T where dipolar-induced mixing is present (evident from the presence of fine structure). The temperature dependence of the EPR features corroborated the presence of a singlet ground state and a triplet excited state, behaving according to eq 8. For large

$$I \propto 1/T[3 + \exp(\Delta E_{S-T}/kT)] \quad (8)$$

values of $\Delta E_{S-T}/kT$, the singlet–triplet gap can be determined from the slope of ln IT vs $1/T$ plots.[34] The $\Delta m = \pm 1$ and ± 2 (slow exchange region) data gave $\Delta E_{S-T} = 0.075 \pm 0.007$ and 0.065 ± 0.007 eV, respectively, in agreement with the value of 0.080 eV determined from magnetic susceptibility (Figure 12).

The zero field splitting parameters calculated from the fine structure splitting ($|D| = 66$, $|E| = 11$ G) are small compared to values reported previously for other 1-D materials, e.g. $(Cs^+)_2(TCNQ)_3^{2-}$,[35] $(Ph_3PMe)^+(TCNQ)_2^-$,[36] $[Co(C_5H_5)_2][DDQ]$[37] (DDQ = 2,3-dichloro-5,6-dicyanobenzoquinone), and [TDAC][DDQ][38] (TDAC = tris(dimethylamino)cyclopropenium). The small splittings in **4** are favored by the non-integral oxidation state that effectively increases the mean distance between dipoles compared to simple $\rho = 1$ salts. Because of the presence of two different TCNQ stacks elucidation of the molecular origin of the triplet species cannot be realized from powder experiments. A more detailed analysis of the EPR behavior of **4**, including a single-crystal study, will be reported elsewhere.[39]

Scheme I

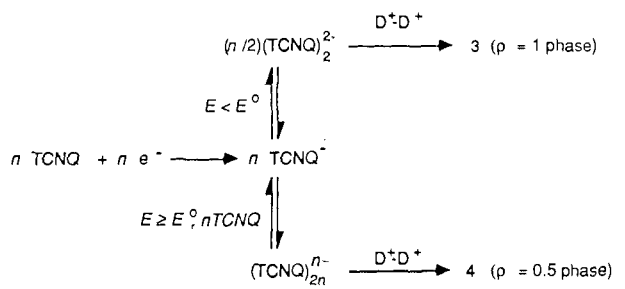

EPR investigations of the $C_3[C(CN)_2]_3^-$ complexes also suggested the presence of energetically accessible triplet species in all these materials, as evidenced by the observation of $\Delta m = \pm 2$ transitions at half-field for all these complexes. Triplet fine structure in the $\Delta m = \pm 1$ region was also readily apparent for **5** even at room temperature; two lines centered around the center field transition are consistent with orthorhombic or higher symmetry and $|D| = 47$ G. For **5** and **6**, the temperature dependences in the $\Delta m = \pm 1$ region indicate triplet excited states with $\Delta E_{S-T} = 0.037$ and 0.025 eV, respectively. However, these observations are in apparent contradiction with the magnetic susceptibility, which indicated that χ did not observably increase with temperature as would be required for the magnitude of the ΔE_{S-T} values determined by EPR. Therefore, the observed triplet species *were not bulk properties*. This apparent discrepancy indicates that the EPR signals can only be attributed to either impurities or defects in **5** and **6**, underscoring the importance of obtaining both EPR and susceptibility data before assigning EPR triplet signals to bulk phenomena.

Discussion

Electrochemical Synthesis. The potential dependent selectivity observed for **3** and **4** is attributed to the different relative concentrations of $TCNQ^0$ and $TCNQ^-$ at the electrode during crystallization at different potentials (as described by the Nernst equation). The $TCNQ^0/TCNQ^-$ ratio affects the relative concentrations of solution entities that eventually evolve into prenucleation aggregates[40] that structurally resemble the motif in the macroscopic crystals. The stoichiometry of the two complexes indicates that **3** possesses $TCNQ^-$ anions that are present exclusively as the singly reduced anion ($\rho = 1$), whereas the mixed valent phase **4** with $\rho = 0.5$ TCNQ stacks formally contains equivalent amounts of $TCNQ^0$ and $TCNQ^-$. This suggests that a $(TCNQ)_2^{2-}$ aggregate precedes crystallization of the $\rho = 1$ phase, whereas a partially reduced TCNQ aggregate such as $(TCNQ)_2^-$ or $(TCNQ)_4^{2-}$, represented generically as $(TCNQ)_{2n}^{n-}$, initiates formation of the $\rho = 0.5$ phase (Scheme I). At very negative potentials the predominant species at the electrode is $TCNQ^-$, favoring the presence of the fully reduced $(TCNQ)_2^{2-}$ dimer dianion. Although it has been demonstrated that the concentration of $(TCNQ)_2^{2-}$ is not significant in nonaqueous solvents containing $TCNQ^-$,[41] fast kinetics for crystallization of **3**, or low concentration of $(TCNQ)_{2n}^{n-}$, can account for the absence of **4** at the more negative potentials. Conversely, when $E \geq E^\circ$ conditions are more favorable for the formation of partially reduced $(TCNQ)_{2n}^{n-}$ aggregates at the electrode surface since $[TCNQ^0] > [TCNQ^-]$ under this condition. The presence of $(TCNQ)_{2n}^{n-}$ aggregates has been corroborated by infrared bands at 2000 cm^{-1} in optically transparent thin-layer electrochemistry experiments,[9] similar to potential dependent behavior reported in EPR studies of electrodes modified with a TCNQ polymer derived from 2,5-bis(2-hydroxyethyl)-7,7,8,8-TCNQ.[42,43]

(34) Wertz, J. E.; Bolton, J. R. *Electron Spin Resonance, Elementary Theory and Practical Applications*; Chapman and Hall: New York, 1986; p 249.
(35) Chesnut, D. B.; Arthur, P., Jr. *J. Chem. Phys.* **1962**, *36*, 2969.
(36) Chestnut, D. B.; Philips, W. D. *J. Chem. Phys.* **1961**, *35*, 1002.
(37) Miller, J. S.; Krusic, P. J.; Dixon, D. A.; Reiff, W. M.; Zhang, J. H.; Anderson, E. C.; Epstein, A. J. *J. Am. Chem. Soc.* **1986**, *108*, 4459.
(38) Radhakrishnan, T. P.; Engen, D. V.; Soos, Z. G. *J. Phys. Chem.* **1987**, *91*, 3273.
(39) Morton, J. R.; Preston, K. F.; Ward, M. D.; Fagan, P. J. *J. Chem. Phys.*, in press.
(40) Addadi, L.; Berkovitch-Yellin, Z.; Weissbuch, I.; van Mil, J.; Shimon, L. J. W.; Lahav, M.; Leiserowitz, L. *Angew. Chem., Int. Ed. Engl.* **1985**, *24*, 466.
(41) Boyd, R. H.; Phillips, W. D. *J. Chem. Phys.* **1965**, *43*, 2927.
(42) Karimi, H.; Chambers, J. Q. *J. Electroanal. Chem.* **1987**, *217*, 313.

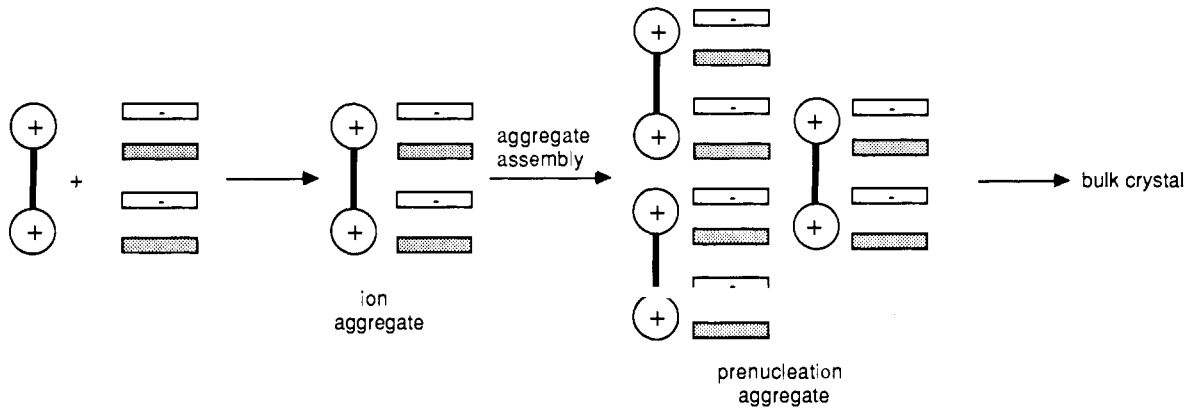

Figure 13. Mechanism for structure enforced crystallization of **4**. The initial step involves formation of an ion aggregate, which is followed by assembly to a prenucleation aggregate that structurally resembles the macroscopic crystal structure. The electrostatic interaction between the polycation and the anions, coupled with π-interactions between anions, results in anion motifs that mimic the spatial arrangement of charge in the polycation.

The potential dependent selectivity is similar to previously reported behavior observed in the electrochemical crystal growth of the organometallic complexes $[(\eta\text{-}C_6Me_6)_2Fe][TCNQ]_x$ (x = 2, 4)[9] and $[Cp^*_2Fe][TCNQ]_x$ (x = 1, 2).[9,15,44] This behavior has also been reported recently for $(HMTP)ClO_4$ (ρ = 1, σ = 0.3 Ω^{-1} cm^{-1}) and $(HMTP)(ClO_4)_2$ (ρ = 2, $\sigma = 10^{-3}$ Ω^{-1} cm^{-1}) [HMTP = hexamethoxytriphenylene)[45] and was briefly mentioned[46] for $TTF(SCN)_{0.59}$ and $TTF(SCN)_{0.64}$, the latter being observed only at more positive electrode potentials. It is apparent that when formation of multiple phases is possible, careful attention to electrochemical parameters during electrocrystallization can allow control of the crystallization process in a rational manner.

Structural Aspects. The solid-state structures of molecular solids result from the molecular nature of the constituents, and intermolecular interactions such as electrostatic forces, van der Waals interactions, covalent linkages, or intermolecular orbital interactions. It is readily apparent from the structural studies of **1–7** that the molecular geometry and the spatial distribution of charge in the cations dramatically affects the solid-state motif and stoichiometry.

The structural enforcement observed in these complexes can be conceptually described on the basis of attractive electrostatic interactions between the cations and anions coupled with the stabilization energy realized from orbital interactions associated with π–π overlap of the planar open-shell radical anions. The initial step in crystallization most likely involves formation of an aggregate consisting of cations and anions. The assembly of the ion aggregate will occur in a manner that maximizes electrostatic attractive forces by bringing the anions into close proximity to the cationic centers. This is depicted in Figure 13 for the evolution of a "1-D" dication and planar anions into the ρ = 0.5 phase **4**. The anion aggregate formed at the electrode aligns parallel to the long axis of the cation, as a result of electrostatic attraction while retaining intermolecular π–π overlap. Growth into larger low-dimensional prenucleation aggregates can then be induced via further π–π interactions between the anions that stabilize the aggregate by electronic delocalization in the more extended arrays. In this way, the ion-pair structures in solution anticipate the solid-state motifs that are realized in the solid.

The effects of concatenated cations is demonstrated by comparison of the solid-state structures of complexes prepared from $\mathbf{D^+}$ and $\mathbf{D^+}$–$\mathbf{D^+}$. In **1**, Madelung stabilization appears to be realized by the close proximity of oppositely charged ions in the ...$\mathbf{D^+A^-D^+A^-}$... chains, as well as by favorable electrostatic interactions between $\mathbf{D^+}$ and $\mathbf{A^-}$ in adjacent stacks. The herringbone arrangement in **2** allows close approach of $\mathbf{D^+}$ to the $\mathbf{A^-A^-}$ dimer within a $\mathbf{D^+A^-A^-D^+}$ fragment, while favorable interactions between segments are suggested by the proximity of a $\mathbf{D^+}$ ion in one fragment to the $\mathbf{A^-A^-}$ dimer of another. Additionally, stabilization from π–π interaction in the $(TCNQ)_2^{2-}$ dimer facilitates the formation of this dimorph. Notably, the ...$\mathbf{D^+D^+A^-A^-D^+D^+A^-A^-}$... motif is not observed here. This motif is uncommon in low-dimensional solids, probably owing to lesser Madelung stabilization compared to the other packing arrangements. However, the presence of concatenated cations in $\mathbf{D^+}$–$\mathbf{D^+}$ allows formation of extended linear chains in **4** with the ...$\mathbf{D^+}$–$\mathbf{D^+A^-A^-D^+}$–$\mathbf{D^+A^-A^-}$... motif.

The effect of length and charge of the $\mathbf{D^+}$–$\mathbf{D^+}$ dication is demonstrated by the non-integral oxidation state observed for the TCNQ molecules in **4**. The average value of the interplanar separation in TCNQ stack A is 3.29 Å, while that in stack B is 3.27 Å. This affords average lengths of 9.87 and 9.81 Å for the $(TCNQ)_4^{2-}$ units in A and B, respectively, well matched to the distance between Cp* planes (9.96 Å) in $\mathbf{D^+}$–$\mathbf{D^+}$ (although these values are slightly less than the axial length of $\mathbf{D^+}$–$\mathbf{D^+}$, this is compensated by a slight cant of the cations with respect to the TCNQ stacking axes). Therefore, *the axial length of the dication accommodates four TCNQ acceptor molecules with interplanar spacing required for intermolecular π–π overlap and orbital interactions. In addition, the presence of two positive charges along the molecular axis of the dication requires only two negative charges for electroneutrality.*

The iron complex $[(C_5H_5)Fe(\eta\text{-}C_6Me_6)^+][(TCNQ)_2^-]$ possesses parallel segregated cation and ρ = 0.5 $TCNQ^{0.5-}$ anion stacks[8] in which two acceptor anions stack along the length of the organometallic cation. The axes of the cations are slightly canted with respect to the TCNQ stacking axis (ca. 15°) and fairly large distances between TCNQ anions are observed (3.35 and 3.37 Å). However, attempts here to prepare the analogous conducting phase $[\mathbf{D^+}][(TCNQ)_2^-]$ failed. This can be attributed to the larger intramolecular ligand separation in $\mathbf{D^+}$ (3.55 Å) compared to the $(C_5H_5)Fe(\eta\text{-}C_6Me_6)^+$ cation (3.26 Å). This would require an increase of >0.1 Å in the interplanar TCNQ separation, reducing the π–π overlap required for stabilization of the extended arrays.[47] Notably, the small 2.85 Å interplanar spacing between the C_4 planes of the cyclophane ligand in $\mathbf{D^+}$ compensates for the larger ruthenium radius so that the distance between Cp* ligands is nearly equivalent to the distance traversed by two colinear $(C_5H_5)Fe(\eta\text{-}C_6Me_6)^+$ cations (9.89 Å).

This structural enforcement of the TCNQ stacks provided by $\mathbf{D^+}$–$\mathbf{D^+}$ in **4** is made manifest in the electrical conductivity and triplet exitonic behavior. The extended anion stacks coupled with charge localization (possibly induced by the cations) allow the formation of triplet excitons. More significantly, the stoichiometric control imposed by the charge/length ratio of the dication results in ρ = 0.5 TCNQ stacks, which favors electrical conductivity compared to simple ρ = 1 salts. However, the activated nature

(43) Inzelt, G.; Day, R. W.; Kinstle, J. F.; Chambers, J. Q. *J. Phys. Chem.* **1983**, *87*, 4592.
(44) Ward, M. D. *Electroanal. Chem.* **1988**, *16*, 181. A. J. Bard, Ed., Marcel Dekker: New York, NY.
(45) Chiang, L. Y.; Johnston, D. C.; Stokes, J. B.; Bloch, A. N. *Synth. Met.* **1987**, *19*, 697.
(46) Lamache, M.; Kacemi, K. E. *Mol. Cryst. Liq. Cryst.* **1985**, *120*, 255.
(47) Garrito, A. F.; Heeger, A. J. *Acc. Chem. Res.* **1974**, *7*, 232.

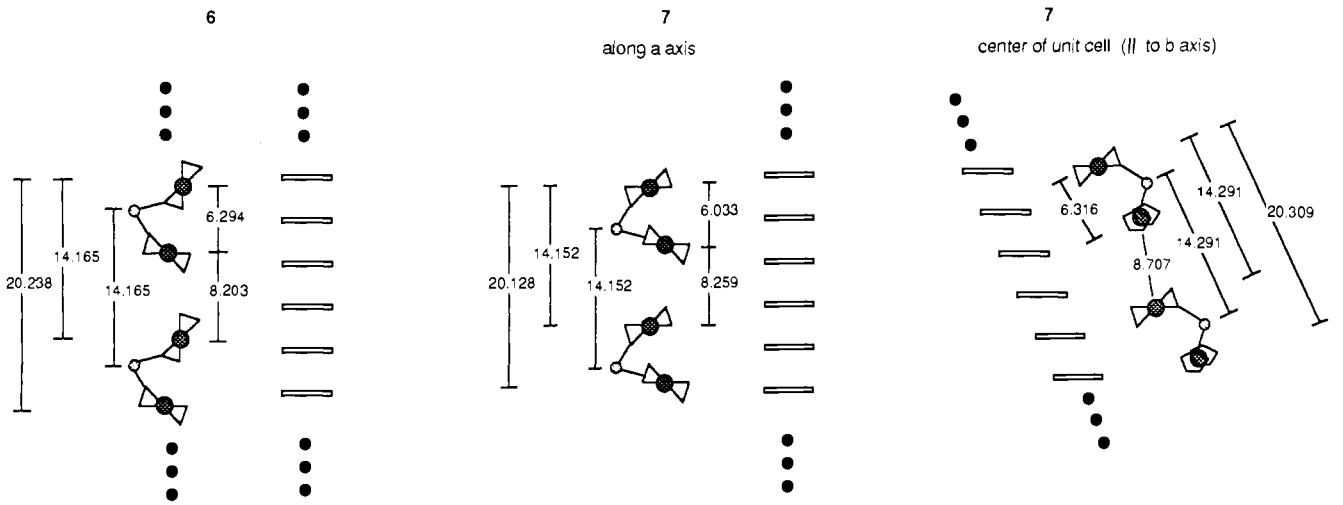

Figure 14. Schematic representation of the relationship between the dipositive Ru^+–Ru^+ axes and the $C_3[C(CN)_2]_3^-$ anion stacks in **6** and **7**. Relevent distances between Ru^+ sites are depicted.

Scheme II

simple salt ($\rho = 1$)

$$\ldots A^- A^- A^- A^- A^- A^- \ldots \longrightarrow \ldots A^- A^- A^0 A^{2-} A^- A^- \ldots$$

mixed valent salt ($\rho = 0.5$)

$$\ldots A^- A^0 A^- A^0 A^- A^0 \ldots \longrightarrow \ldots A^- A^0 A^0 A^- A^- A^0 \ldots$$

of the conductivity suggests the persistence of Coulomb repulsion energies between charge carriers that exceed the bandwidth.[48] If conduction is viewed as a site-hopping mechanism, in a $\rho = 1$ stack Coulomb correlations lead to semiconducting behavior owing to the Coulomb repulsions between charges associated with a single A^{2-} site (Scheme II), resulting in formation of a Mott–Hubbard semiconductor. Under these conditions the activation energy is that needed for electronic transitions across an energy gap created by the Coulomb correlation, i.e., the Mott transition energy.

Conversely, the non-integral ρ value in **4** results in higher conductivity since site hopping can occur without the formation of doubly occupied sites. The Coulomb correlations that give rise to the observed activated behavior result from charge localization within the stacks, as evidenced by the crystallographic inequivalence of the TCNQ acceptors and the periodic motif of the TCNQ stacks. In molecular terms, the charge localization can be conceptually described by $\ldots(AAAA)^{2-}(AAAA)^{2-}\ldots$ sites. The activation energy is that required to overcome Coulombic repulsion associated with formation of $\ldots(AAAA)^{-}(AAAA)^{3-}\ldots$ sites during charge transport. The relatively small activation energy observed for **4** compared to simple $\rho = 1$ TCNQ salts is attributed to the larger size of the aggregate upon which localization occurs (i.e. one negative charge per two TCNQ molecules), which substantially reduces the Coulomb repulsion energy.[49] The presence of two different TCNQ acceptor stacks complicates delineation of the origin of the conductivity. However, it seems reasonable to suggest that stack B plays a more significant role in the electronic conductivity owing to the more uniform spacing of the TCNQ molecules.

The effect of different spatial distributions of charge in the polycations is even more apparent when comparing the complexes containing the $C_3[C(CN)_2]_3^-$ anion. Investigation of these as well as other complexes[28,31a] containing the $C_3[C(CN)_2]_3^-$ anion reveals that this acceptor is disposed toward the formation of linear chains. Whereas the linear geometry of D^+–D^+ induces the formation of parallel linear chains of anions and cations in **5**, $(D^+)_4E$ cations induce stacking of the anions into mutually orthogonal chains in **6** and **7** that are aligned parallel to the orthogonal axes defined by the two pairs of cationic Ru sites within each of the tetracations. In the case of **6** and **7**, this results in formation of complexes with pronounced anisotropy in two dimensions and hence a "2-D" motif. This behavior can be readily understood on the basis of the aggregate model discussed above where one would expect the initial ion paired complex to be composed of two mutually perpendicular pairs of anions per tetracation. The electronic stabilization realized through extended π–π overlap of the open-shell anions leads to formation of the extended solid with stacking along the axes defined by the two pairs of cationic centers in the aggregate.

The distance between the intramolecular Ru^+ sites that define these dipositive axes of charge in **6** and **7** is roughly equivalent to the distance required to accommodate two $C_3[C(CN)_2]_3^-$ anions. The relevant structural features are schematically depicted in Figure 14. The intermolecular distance between Ru^+ sites on neighboring cations in a stack is slightly larger owing to the steric bulk of the Cp* ligands. This results in a distance between symmetry related Ru^+ sites of approximately 14 Å, which is that required to accommodate four anions with an approximate 3.5-Å interplanar separation. Indeed, the average separation between anions approached 3.4 Å in both **6** and **7**, whereas much smaller interplanar separations (ca. 3.2 Å) for these anions have been observed in other charge transfer solids.[28] It may be expected that expanding the size of the tetracation by substitution of the central E atom would systematically increase the interplanar spacing between $C_3[C(CN)_2]_3^-$ anions. This would presumably be manifested by equally systematic changes in the electronic properties. However, correlations of this type in **6** and **7** are somewhat complicated by slight, but different degrees of, rotation of the Ru^+–Ru^+ axes relative to the anion which serves to shorten the effective distance between charges when viewed strictly along the stacking axis. Due to the different extents of this rotation the interplanar spacing does not follow any trend that may be expected from the distance between intramolecular Ru^+–Ru^+ sites, or from the repeat distance between tetracations. For example, in **7** the average interplanar distance between anions in the stack along the *a* axis actually is larger than the interplanar stacking in the stack parallel to the *b* axis, although the intramolecular Ru^+–Ru^+ and tetracation repeat distances are smaller in the former. This suggests that more precise predictions of solid-state features, such as spacing between acceptor species, may be reserved for linear polycations, which are less prone to this behavior.

Conclusions

The charge transfer complexes described here clearly demonstrate that the three-dimensional solid-state structure can be rationally controlled by designed electrostatic interactions between polycations of known dimensionality and planar acceptor anions.

(48) (a) Torrance, J. B. *Acc. Chem. Res.* **1979**, *12*, 79. (b) Garito, A. F.; Heeger, A. J. *Acc. Chem. Res.* **1973**, *7*, 232.

(49) Edwards, P. P.; Sienko, M. J. *Phys. Rev.* **1978**, *17*, 2575.

Table III. X-ray Experimental Details for $Cp^*Ru(C_6Me_6)^+$–$TCNQ^-$ Complexes **1** and **2**

	1	**2**
molecular formula	$C_{34}H_{37}RuN_4$	$C_{34}H_{37}RuN_4$
formula weight	602.77	602.77
crystal dimnsn, mm	0.28 × 0.35 × 0.42	0.35 × 0.37 × 0.56
peak width at half-height, deg	0.35	0.34
source	Mo Kα (λ = 0.71073 Å)	Cu Kα (λ = 1.54184 Å)
temp, °C	−25 (1)	−40 (1)
space group	$P\bar{1}$	$P2_1/c$
a, Å	8.975 (9)	9.883 (2)
b, Å	9.830 (3)	12.359 (4)
c, Å	10.375 (5)	23.743 (2)
α, deg	64.79 (3)	
β, deg	64.12 (8)	94.21 (1)
γ, deg	75.20 (6)	
V, Å^3	742.4 (6)	2892 (2)
z	1	4
ρ, g/cm^3	1.35	1.38
μ, cm^{-1}	5.4	46.9
attenuators	Zr foil, factor 19.4	Ni foil, factor 21.1
take-off angle, deg	2.8	2.8
detector aperture:	2.0 to 2.4 mm horizontal, 4.0 mm vertical	2.0 to 3.5 mm horizontal, 4.0 mm vertical
crystal-detector dist, cm	21	21
scan type	ω–θ	ω–θ
scan rate, deg/min	2–5 (in ω)	2–5 (in ω)
scan width, deg	1.0 + 0.140 tan θ	1.1 + 0.140 tan θ
max 2θ, deg	45.0	112.0
no. of refl. measured	1941, total, 1879 unique	4216 total, 3650 unique
corrections	Lorentz-polarization linear decay (from 0.989 ω 1.222 on I)	Lorentz-polarization linear decay from (0.982 ω 1.091 on I)
solution	Patterson method	direct method
hydrogen atoms	included as fixed contribution to the structure factor	included as fixed contribution to the structure factor
anomalous dispersion	all non-hydrogen atoms	all non-hydrogen atoms
reflcns included	1876 with $F_o^2 > 2.0\sigma(F_o^2)$	3536 with $F_o^2 > 2.0\sigma(F_o^2)$
parameters refined	205	342
unweighted agreement factor	0.031	0.050
weighted agreement factor	0.036	0.060
esd of obs of unit weight	0.72	4.56
convergence, largest shift:	0.02σ	0.25σ
high peak in final diff map, e/Å^3	0.44 (5)	0.94 (9)

Table IV. X-ray Experimental Details for $[(Cp^*Ru)_2(\eta^6,\eta^6\text{-}[2_2](1,4)\text{cyclophane})^{2+}][(TCNQ)_x^{2-}]$ Complexes **3** and **4**

	3 (x = 2)	**4** (x = 4)
molecular formula	$C_{60}H_{54}Ru_2N_8$	$C_{84}H_{62}Ru_2N_{16}$
formula weight	1089.29	1497.73
crystal dimns, mm	0.16 × 0.40 × 0.48	0.10 × 0.21 × 0.76
peak width at half-height, deg	0.21	0.28
source	Mo Kα (λ = 0.71073 Å)	Mo Kα (λ = 0.71073 Å)
temp, °C	−25 (1)	−25
space group	$P\bar{1}$	$P\bar{1}$
a, Å	8.553 (3)	13.963 (5)
b, Å	12.168 (2)	16.107 (3)
c, Å	13.961 (5)	16.855 (5)
α, deg	66.67 (3)	67.60 (2)
β, deg	72.56 (3)	87.30 (4)
γ, deg	72.27 (2)	81.41 (2)
V, Å^3	1243.9 (6)	3465.2
z	1	2
ρ, g/cm^3	1.45	1.435
μ, cm^{-1}	6.4	4.84
attenuator	Zr foil, factor 21.1	Zr foil, factor 21.1
take-off angles, deg	2.8	2.8
detector aperture	2.0 to 2.4 mm horizontal, 4.0 mm vertical	2.0 to 2.4 mm horizontal, 4.0 mm vertical
crystal-detector dist, cm	21	21
scan type:	ω–θ	ω–θ
scan rate, deg/min	2–5 (in ω)	2–5 (in ω)
scan width, deg	1.0 + 0.140 tan θ	1.0 + 0.140 tan θ
max 2θ, deg	46.0	46.0
no. of reflcns measured	2614 total, 2531 unique	9628 total, 7544 unique
corrections	Lorentz-polarization linear decay (from 0.955 to 1.113 on I)	none
solution	direct methods	Patterson
hydrogen atoms	refined with B_{iso} = 5.0 Å	included as fixed positions
anomalous dispersion	all non-hydrogen atoms	all non-hydrogen atoms
reflections included	2471 with $F_o^2 > 2.0\sigma(F_o^2)$	7544 with $F_o^2 > 3.0\sigma(F_o^2)$
parameters refined	352	919
unweighted agreement factor	0.028	0.045
weighted agreement factor	0.032	0.061
esd of obs of unit weight	1.07	2.59
convergence, largest shift	0.03σ	
high peak in final diff map e/Å^3	0.33 (5)	0.74

The stoichiometry of charge transfer complexes and the degree of charge on molecular components can be rationally controlled by the charge and size (length) of the polycation, as well as by the electrochemical parameters during electrocrystallization of these complexes. The structural enforcement is reminiscent of other low-dimensional solids in which the size and charge of attendant counterions dramatically affects structure and electronic properties. For example, the anion size and symmetry has been reported to play an important role in the structure and electronic properties of superconducting β-(bisethylenedithiotetrathiafulvalene)$_2$X (X = I_3^-, I_2Br^-, IBr_2^-, AuI_2^-)[50] and (tetramethyltetraselenafulvalene)$_2$X salts,[51] and metallophthalocyanine complexes.[52] The properties of the former series, particularly the superconducting transition temperature, are affected by differences in lattice pressure exerted by the differently sized linear anions. Similar reasoning would suggest that adjustment of the distance between charged centers within the polycations described here would result in variation of the distance between acceptor anions in molecular solids and accordingly "tuning" of their electronic properties. For example, by replacing $\mathbf{D}^+$–$\mathbf{D}^+$ with $Cp^*Ru(\eta^6,\eta^6[2_2](1,4)cyclophane)CoCp^{*3+}$, $(Cp^*Fe)_2(\eta^6,\eta^6\text{-}[2_2](1,4)cyclophane)^{2+}$, or $[Cp^*Ru(\eta^6,\eta^6\text{-}[2_2](1,4)\text{-}cyclophane)]_2Ru^{4+}$ one can envision control of the stoichiometry and interplanar separations between acceptor molecules, with attendant changes in electronic properties. Investigations toward this goal are currently in progress.

(50) (a) Emge, T. J.; Leung, P. C. W.; Beno, M. A.; Wang, H. H.; Firestone, M. A.; Webb, K. S.; Carlson, K. D.; Williams, J. M. *Mol. Cryst. Liq. Cryst.* **1986**, *132*, 363. (b) Wang, H. H.; Beno, M. A.; Geiser, U.; Firestone, M. A.; Webb, K. S.; Nunez, L.; Crabtree, G. W.; Carlson, K. D.; Williams, J. M.; Azevedo, L. J.; Kwak, J. F.; Schirber, J. E. *Inorg. Chem.* **1985**, *24*, 2465.

(51) Kistenmacher, T. J. *Mol. Cryst. Liq. Cryst.* **1986**, *136*, 361.

(52) Palmer, S. M.; Stanton, J. M.; Hoffman, B. M.; Ibers, J. A. *Inorg. Chem.* **1986**, *25*, 2296.

Experimental Section

Materials. Acetonitrile was distilled from CaH_2 and nitromethane from $CaSO_4$ under nitrogen. Tetra-*n*-butylammonium tetrafluoroborate was recrystallized from ethyl acetate–ethanol and dried in vacuo prior to use.

Equipment. All manipulations were performed under inert atmosphere conditions with purified nitrogen and a Vacuum Atmospheres glovebox.

Table V. X-ray Experimental Details for $C_3[C(CN)_2]_3^-$ Complexes **5–7**

	5	**6**	**7**
empirical formula	$C_{60}H_{46}N_{12}Ru_2$	$C_{119}H_{98}N_{30}O_{12}R_4$	$C_{116}H_{92}N_{28}SiO_8Ru_4$
formula weight	1137.24	2544.69	2438.69
crystal dimensions, mm	0.20 × 0.15 × .35	0.33 × 0.25 × 0.52	0.47 × 0.17 × 0.47
peak width at half height, deg	0.28	0.15	0.15
source	Cu Kα (λ = 1.54178 Å)	Mo Kα (λ = 0.71073 Å)	Mo Kα (λ = 0.71073 Å)
temp, °C	23	−70	−70
space group	$P2_1/a$ (No. 14)	$C2/c$ (No. 15)	$P\bar{1}$
a, Å	13.746 (4)	20.720 (10)	14.152 (3)
b, Å	24.686 (1)	19.320 (10)	14.292 (2)
c, Å	15.711 (1)	30.890 (20)	29.054 (6)
α, deg			81.54 (2)
β, deg	100.66 (2)	107.48 (5)	78.24 (2)
γ, deg			79.13 (2)
V, Å^3	5240 (2)	11794.6	5613.7
Z, g/cm^3	4	4	2
ρ(calc), g/cm^3	1.44	1.433	1.442
μ, cm^{-1}	52.72	5.62	5.94
take-off angle, deg	6.0	2.35	2.35
scan type	ω–2θ	ω–2θ	ω–2θ
scan rate, deg/min	5.3–16.0	1.50–5.00	1.50–5.00
scan width, deg ω	(0.89 + 0.30 tan θ)	1.20–1.50	1.20–1.80
max 2θ, deg	118.0	50.0	48.0
no. of reflcns measured	7636 total	10913 total	22240
corrections	Lorentz-polarization absorption (trans. factors: 0.81–1.00) (Secondary Extinction coefficient 0.17691 E–06)	Lorentz-polarization	Lorentz-polarization
solution	direct methods	Patterson	Patterson
hydrogen atoms	included in calculated positions (d_{C-H} = 0.95 Å)	included in calculated positions (d_{C-H} = 0.95 Å)	included in calculated positions (d_{C-H} = 0.95 Å)
"ignorance" factor	0.05	0.03	0.03
anomalous dispersion	all non-hydrogen atoms	Ru	Ru
reflcns included	3774 with $F_o^2 > 3.0\sigma(F_o^2)$	4801 ($I > 3\sigma(I)$)	9184(I) > $3\sigma(I)$
parameters refined	668	680	1338
unweighted agreement factor	0.043	0.069	0.054
weighted agreement factor	0.051	0.063	0.049
esd of obs of unit weight	1.13	1.67	1.40
convergence, largest shift	0.22	0.54	0.61
high peak in final diff map, e$^-$/Å^3	0.59	0.71 (solvent)	0.69 (solvent)

Electrocrystallizations were performed in a standard H-cell with a glass fritted separator with an Ag/AgCl reference electrode (Bio-Analytical Systems, Inc.) and platinum foils (0.5 × 0.5 cm) as the working and auxiliary electrodes. A Princeton Applied Research 173 potentiostat was used when coulometric determinations were required and a Modell 440 multichannel potentiostat from the Electrosynthesis Corporation was used for routine syntheses. Infrared spectra were recorded on a Nicolet 7199 Fourier Transform spectrometer. EPR studies were performed on an X-band Bruker ER200D-SRC spectrometer.

Magnetic susceptibility data were collected over the range 1.8–325 K with use of a high-sensitivity computer interfaced Faraday balance. Samples were suspended on a 1-mm quartz rod from the arm of a Cahn 1000 electrobalance. The sample container (4.2 × 10 mm) was fashioned from high-purity Spectrosil quartz. An electromagnet (Walker Scientific) supplied variable fields up to 22.5 kG. The magnetic field gradient was calibrated with $HgCo(SCN)_4$ as a standard and varied by less than 1% in the area of the sample container. Temperature was controlled with a digital temperature controller (Oxford Instruments 3120) with use of a Au/Fe versus chromel P thermocouple. A calibrated silicon diode resistance thermometer was used to measure the sample temperature, independently of the controlling thermocouple, over the entire temperature range. The Cahn balance was operated on the 100-mg scale, on which a sensitivity in ideal conditions of 0.001 mg can be achieved. In normal operating conditions the sensitivity is the larger of 0.02 mg or 0.1% of the force being measured. A typical error estimate in the measurement of the susceptibilities reported in this paper is 0.5%. The susceptibilities have been corrected for the intrinsic diamagnetism of the sample container and the diamagnetism of the electronic cores of the constituent atoms.

Conventional Synthesis of [Cp*Ru(η-C_6Me_6)$^+$][TCNQ$^-$] 1-D Phase (1). Analytically pure **1** was prepared by slow addition of (n-Bu_4N^+)(TCNQ$^-$) (40 mg, 0.09 mmol) in 5 mL of acetonitrile to [Cp*Ru(η-C_6Me_6)$^+$]($O_3SCF_3^-$) (50 mg, 0.09 mmol) in 5 mL of acetonitrile. The precipitate was washed three times with 5 mL of acetonitrile and dried in vacuo to yield emerald green microcrystalline **1** in quantitative yield. Anal. Calcd: C, 67.75; H, 6.19; N, 8.29. Obsd: C, 67.93; H, 6.03; N, 8.49. Alternatively, **1** could be prepared as a fibrous polycrystalline material by slow diffusion methods in acetonitrile.

Electrocrystallization of 1. [Cp*Ru(η-C_6Me_6)$^+$]($O_3SCF_3^-$) (50 mg, 0.09 mmol) and TCNQ (40 mg, 0.20 mmol) were added to the working compartment of a H-cell containing a nitromethane solution of 0.1 M (n-Bu_4N^+)(BF_4^-) in both compartments. Platinum electrodes were inserted in both compartments and an Ag/AgCl reference inserted in the working side. The cell was biased at +0.2 V, upon which the solution in the vicinity of the electrode became light green in color. After approximately 1 h, green crystals were evident on the electrode. After 1.75 C had passed through the cell (10% conversion to **1**), the crystals were harvested by filtration and washed carefully three times with cold nitromethane (9.3 mg; 78% Faradaic yield).

Synthesis of [Cp*Ru(η-C_6Me_6)$^+$]$_2$[TCNQ$^-$]$_2$ Dimer Phase (2). A solution of (n-Bu_4N^+)(TCNQ$^-$) (40 mg, 0.20 mmol) in 5 mL of acetonitrile was allowed to slowly diffuse into a solution of [Cp*Ru(η-C_6Me_6)$^+$]($O_3SCF_3^-$) (50 mg, 0.09 mmol) in 10 mL of acetonitrile over a period of 2 weeks. The major product was **1**, which was obtained as a fibrous green polycrystalline solid. The dimer phase **2**, which constituted less than 5% of the total product, was present as large purple crystals with a triclinic habit. After the crystals were washed with cold acetonitrile, **2** was manually separated from **1**.

Electrocrystallization of [(Cp*Ru)$_2$(η^6,η^6-[2$_2$](1,4)cyclophane)$^{2+}$][TCNQ$^-$]$_2$ (3). [(Cp*Ru)$_2$(η^6,η^6-[2$_2$](1,4)cyclophane)$^{2+}$]($O_3SCF_3^-$)$_2$ (41 mg, 0.045 mmol) and TCNQ (40 mg, 0.20 mmol) were added to the working compartment of a H-cell containing a nitromethane solution of 0.1 M (n-Bu_4N^+)(BF_4^-) in both compartments. Platinum electrodes were inserted in both compartments and an Ag/AgCl reference inserted into the working compartment. The cell was biased at −0.1 V (vs SCE), upon which purple crystals formed immediately on the electrode. After 18 h 1.80 C had passed through the cell (20% conversion) and the product was harvested by filtration and washed three times with nitromethane to yield

X-ray quality crystals of **3** (9.4 mg, Faradaic yield = 96%). Anal. Calcd: C, 66.16; H, 5.00; N, 10.29. Obsd: C, 65.78; H, 4.76; N, 10.45.

Electrocrystallization of $[(Cp^*Ru)_2(\eta^6,\eta^6\text{-}[2_2](1,4)cyclophane)^{2+}][(TCNQ)^{2-}]_4$ (4). $[(Cp^*Ru)_2(\eta^6,\eta^6\text{-}[2_2](1,4)cyclophane)^{2+}](O_3SCF_3^-)_2$ (41 mg, 0.045 mmol) and TCNQ (40 mg, 0.20 mmol) were added to the working compartment of a H-cell containing a nitromethane solution of 0.1 M $(n\text{-}Bu_4N^+)(BF_4^-)$. Platinum electrodes were inserted in both compartments and an Ag/AgCl reference inserted into the working compartment. The cell was biased at +0.4 V (vs SCE) and left to stand for several days. Black needle shaped crystals slowly grew on the electrode. After approximately 1 week 1.80 C had passed through the cell (20% conversion to **4**) and the product was harvested by filtration and washed three times with nitromethane to yield X-ray quality crystals of **4** (13.2 mg, Faradaic yield = 98%). Anal. Calcd: C, 67.37; H, 4.17; N, 14.96. Obsd: C, 67.47; H, 4.16; N, 15.00.

Synthesis of $[(Cp^*Ru)_2(\eta^6,\eta^6\text{-}[2_2](1,4)cyclophane)^{2+}]\{C_3[C(CN)_2]_3^-\}^2$ (5). A solution of $(n\text{-}Bu_4N^+)\{C_3[C(CN)_2]_3^-\}$ (40 mg, 0.09 mmol) and $[(Cp^*Ru)_2(\eta^6,\eta^6\text{-}[2_2](1,4)cyclophane)^{2+}](O_3SCF_3^-)_2$ (41 mg, 0.045 mmol) in 3 mL of acetonitrile was allowed to stand at 10 °C for a period of 2 weeks. Filtration of the dark blue solution yielded small, dark purple needles, which after careful washing with cold acetonitrile gave **5** in 30% yield. Anal. Calcd: C, 63.37; H, 4.08; N, 14.78. Obsd: C, 63.75; H, 4.23; N, 14.36.

Synthesis of $\{[Cp^*Ru(\eta\text{-}C_6H_5)]_4C^{4+}\}\{C_3[C(CN)_2]_3^-\}_4\cdot 6CH_3NO_2$ (6). A solution of $(n\text{-}Bu_4N^+)\{C_3[C(CN)_2]_3^-\}$ (37 mg, 0.08 mmol) and $\{[Cp^*Ru(\eta\text{-}C_6H_5)]_4C^{4+}\}(O_3SCF_3^-)_4$ (37 mg, 0.020 mmol) in 3 mL of acetonitrile was allowed to stand at 10 °C for a period of 2 weeks. Filtration of the dark blue solution yielded dark purple, large rhombic shaped crystals that after careful washing with cold acetonitrile gave **6** in 20% yield. Anal. Calcd: C, 56.17; H, 3.88; N, 16.51. Obsd: C, 55.84; H, 3.85; N, 15.97.

Synthesis of $\{[Cp^*Ru(\eta\text{-}C_6H_5)]_4Si^{4+}\}\{C_3[C(CN)_2]_3^-\}_4\cdot 4CH_3NO_2$ (7). A solution of $(n\text{-}Bu_4N^+)\{C_3[C(CN)_2]_3^-\}$ (37 mg, 0.08 mmol) and $\{[Cp^*Ru(\eta\text{-}C_6H_5)]_4Si^{4+}\}(O_3SCF_3^-)_4$ (37 mg, 0.020 mmol) in 3 mL of acetonitrile was allowed to stand at 10 °C for a period of 2 weeks. Filtration of the dark blue solution yielded dark purple, platelike crystals that after careful washing with cold acetonitrile gave **7** in 20% yield. Anal. Calcd: C, 57.14; H, 3.80; N, 16.08. Obsd: C, 56.65; H, 3.93; N, 15.62.

X-ray Data Collection and Data Reduction.[53] Preliminary examination and data collection were performed on an Enraf-Nonius CAD4 computer controlled kappa axis diffractometer equipped with a graphite crystal, incident beam monochromator. Tables III–V summarize the relevent conditions of data collection.

As a check on crystal and electronic stability three representative reflections were measured every 30 min. The intensities of these standards changed for all the complexes and an anisotropic decay correction was applied (see tables).

Structure Solution and Refinement. Relevent conditions are summarized in Tables III–V. The structures were solved by either direct or Patterson methods. The structures were refined in full-matrix least-squares where the function minimized was $\sum w(|F_o| - |F_c|)^2$ and the weight w is defined as $4F_o^2/\sigma^2(F_o^2)$. The standard deviation on intensities is $\sigma^2(F^2_o) = [S^2(C + R^2B) + (pF^2_o)^2]/L_p^2$, where S is the scan rate, C is the total integrated peak count, R is the ratio of scan time to background counting time, B is the total background count, L_p is the Lorentz–polarization factor, and the parameter p (ignorance factor) is a factor introduced to downweight intense reflections.

Scattering factors were taken from Cromer and Waber.[54] Anomalous dispersion effects were included in F_c;[55] the values for $\Delta f'$ and $\Delta f''$ were those of Cromer.[56] The final cycle of refinement converged with unweighted and weighted agreement factors according to

$$R_1 = \sum||F_o| - |F_c|/\sum|F_o|$$

$$R_2 = (\sum w(|F_o| - |F_c|)^2/\sum wF_o^2)^{1/2}$$

The highest peaks in the final difference Fourier and the estimated errors based on ΔF[57] are given in the tables. Plots of $\sum w(|F_o| - |F_c|)^2$ versus $|F_o|$, reflection order in data collection, sin (q/l), and various classes of indices showed no unusual trends for any of the compounds.

Acknowledgment. The authors thank E. J. Delawski and R. S. McLean for technical assistance.

Supplementary Material Available: X-ray structural reports for **1–7** containing descriptions of experimental procedures that include data collection, data reduction, and structure solution and refinement, tables of crystal data, intensity measurements, structure solution and refinement, positional and thermal parameters, general temperature factor expressions (U's), bond distances, bond angles, torsional angles, root-mean-square (rms) amplitudes of thermal vibrations, tables of intermolecular contacts, least-squares planes, drawings of individual cations and anions with labeling schemes, and stereoviews (183 pages). Ordering information is given on any current masthead page.

(53) The complete structural determination of **1**, **2**, and **3** and data collection for **4** were performed by Oneida Research Services, Inc. Structural determination of **5** was performed by Molecular Structure Corporation. The structural refinement of **4** and structural determination of **6** and 7 was performed by JCC.

(54) Cromer, D. T.; Waber, J. T. *International Tables for X-Ray Crystallography*; The Kynoch Press: Birmingham, England, 1974; Vol. IV, Table 2.2B.

(55) Ibers, J. A.; Hamilton, W. C. *Acta Crystallogr.* **1964**, *17*, 781.

(56) Cromer, D. J. *International Tables for X-Ray Crystallography*; The Kynoch Press: Birmingham, England, 1974; Vol. IV, Table 2.3.1.

(57) Cruickshank, D. W. J. *Acta Crystallogr.* **1949**, *2*, 154.